



**HAL**  
open science

## Modeling of fluid-induced seismicity during injection and after shut-in

Qinglin Deng, Guido Blöcher, Mauro Cacace, Jean Schmittbuhl

► **To cite this version:**

Qinglin Deng, Guido Blöcher, Mauro Cacace, Jean Schmittbuhl. Modeling of fluid-induced seismicity during injection and after shut-in. *Computers and Geotechnics*, 2021, 140, pp.104489. 10.1016/j.compgeo.2021.104489 . hal-03873870

**HAL Id: hal-03873870**

**<https://hal.science/hal-03873870>**

Submitted on 16 Oct 2023

**HAL** is a multi-disciplinary open access archive for the deposit and dissemination of scientific research documents, whether they are published or not. The documents may come from teaching and research institutions in France or abroad, or from public or private research centers.

L'archive ouverte pluridisciplinaire **HAL**, est destinée au dépôt et à la diffusion de documents scientifiques de niveau recherche, publiés ou non, émanant des établissements d'enseignement et de recherche français ou étrangers, des laboratoires publics ou privés.



Distributed under a Creative Commons Attribution - NonCommercial 4.0 International License

16 Modeling of fluid-induced seismicity during injection  
17 and after shut-in

18 Qinglin Deng<sup>1,\*</sup>, Guido Blöcher<sup>2</sup>, Mauro Cacace<sup>2</sup>, Jean Schmittbuhl<sup>1</sup>

---

19 **Abstract**

We develop a fully coupled hydro-mechanical model to simulate fault slip due to fluid injection. We consider the interaction between a hydraulic fracture and pre-existing faults as well as the fluid exchange between the fracture/fault and the porous matrix. In order to consider a pressure diffusion mechanism, we set a relatively high permeability around the stimulated path. Our parametric study shows that a couple of factors affect the fault activation and its slip behavior such as fault properties, friction properties and injection scenario. We observe that pore pressure diffusion induces poroelastic stress change, which are able to produce shut-in events with a time and space lag. This mechanism also affects the slip behavior during injection in particular when the surrounding permeability is high (e.g., up to  $1e-13$  m<sup>2</sup>/s), and provides a new insight into understanding the occurrence of stronger seismic events after shut-in compared to the injection phase. In addition, we show that small perturbations may trigger large seismic fault slip which highlights the key role of the initial fault stress state. The results have profound implications for deep fluid injection related engineering as well as for soft cyclic injection strategies aiming to mitigate the risk of large earthquakes.

20 *Keywords:* hydraulic stimulation, hydro-mechanical coupling, fault  
21 reactivation, induced seismicity, pore pressure diffusion, shut-in effect

---

\*Corresponding author

*Email address:* [dengq@unistra.fr](mailto:dengq@unistra.fr) (Qinglin Deng)

<sup>1</sup>EOST/ITES, Université de Strasbourg/CNRS, France

<sup>2</sup>GFZ German Research Centre for Geosciences, Potsdam, Germany

---

## 22 1. Introduction

23 Hydraulic stimulation has been applied in many underground engineer-  
24 ing projects, such as coalbed methane mining (McDaniel et al., 1990; Col-  
25 menares and Zoback, 2007), oil/gas recovery (Law et al., 1993; Barati and  
26 Liang, 2014), shale gas production (Johri and Zoback, 2013; Lei et al., 2017),  
27 waste water disposal (Keranen et al., 2014; Brudzinski and Kozłowska, 2019)  
28 as well as deep geothermal energy extraction (Fehler, 1989; Murphy et al.,  
29 1999; Evans et al., 2005; Gaucher et al., 2015; Schill et al., 2017). It has been  
30 proven to be effective to improve fracture connectivity, increase reservoir  
31 transmissivity and enhance fluid circulation. However, due to high pressure  
32 fluid injection, such operation is often accompanied by seismic activities.  
33 Sometimes they can be felt by people on the ground and destroy ground  
34 facilities, therefore cause strong social disputes (Majer et al., 2007; Häring  
35 et al., 2008; Langenbruch et al., 2018; Lee et al., 2019; Lei et al., 2019). Fur-  
36 thermore, those man-made earthquakes not only occur during the injection  
37 phase, but also after the operation termination, termed as ‘post injection  
38 induced seismicity’, which can be observed both from the laboratory and  
39 the field (Stanchits et al., 2011; Hsieh and Bredehoeft, 1981; Evans et al.,  
40 2005; Albaric et al., 2014). The post injection induced seismicity sometimes  
41 exhibits discontinuities both in time and space. For instance, the hydraulic  
42 stimulation performed in June 2013 in the Rittershoffen geothermal site in-  
43 duced seismicity during injection but a second swarm of events occurred  
44 over 100 meters away from the first earthquake sequence 4 days after shut-  
45 in (Lengliné et al., 2017). Moreover, these additional seismic events may

46 have large magnitude, some of them are even stronger than the seismicity  
47 during the injection (Häring et al., 2008; Baisch et al., 2010; Albaric et al.,  
48 2014; McClure, 2015; Baujard et al., 2017). Those observations increase the  
49 uncertainty and complexity of the hydraulic operation response, and pose a  
50 challenge for earthquake risk prediction and control.

51 Over the past few decades, a large number of researchers have been de-  
52 voted to study fluid-induced seismicity mechanisms and its hazard control,  
53 across scales ranging from  $\sim$  cm to  $\sim$  km. Those studies are based on either  
54 a statistical (Shapiro et al., 1999; Parotidis et al., 2004; Barth et al., 2013)  
55 or physical description of the induced dynamics. Physics based investigation  
56 comprises laboratory experiments (Stanchits et al., 2011; Passelègue et al.,  
57 2018; Ji et al., 2019; Wang et al., 2020), field tests (Cornet and Jianmin,  
58 1995; Blöcher et al., 2018; De Barros et al., 2019), as well as numerical mod-  
59 eling (Baisch et al., 2010; Yoon et al., 2017; Maurer et al., 2020). The main  
60 triggering mechanisms for injection-induced seismicity, can be attributed to  
61 pore pressure diffusion (Shapiro et al., 1999; Brown and Ge, 2018), poroelastic  
62 stress response (McClure and Horne, 2011; Chang and Segall, 2016; Jacquy  
63 et al., 2018), aseismic slip (Guglielmi et al., 2015; Lengliné et al., 2017), as  
64 well as earthquake interactions (Yeo et al., 2020). Yet other mechanisms are  
65 also reported to be responsible for post-injection induced seismicity, such as  
66 the superposed stress variations (De Simone et al., 2017) and fracture normal  
67 closure (Ucar et al., 2017).

68 Although those studies have formed the basic framework of fluid injection  
69 induced seismicity, none of them can deal with all cases due to the complexity  
70 of the underground structure and the coupling process. Some questions, e.g.,

71 the role of related control parameters, have been partially answered and still  
72 need to be further investigated. Thus, it is of primary importance to explore  
73 the multi-physical processes undergoing in deep reservoirs from the injection  
74 stage to the post injection stage, in order to minimize the risk of earthquakes  
75 and achieve successful hydraulic stimulation.

76 The goal of a hydraulic stimulation is to stimulate permeability enhance-  
77 ment in the reservoir. As such it requires a good conceptual model for the  
78 stimulation. Currently, there are four main stimulation mechanisms are con-  
79 sidered: (i) pure opening (tensile) mechanism, aiming to create new fractures  
80 (i.e., hydro-fracturing) (Zoback et al., 1977; Ren et al., 2015); (ii) pure shear  
81 mechanism, which assumes that the stimulation mainly acts on the shear slip  
82 of the pre-existing fractures (Xie and Min, 2016; Ye and Ghassemi, 2018); (iii)  
83 primary fracturing with shear stimulation leakoff, under which new fractures  
84 are continuously created and propagated from the wellbore with fluid leaks  
85 off into natural fractures (Pearson, 1981; Wang et al., 2018); (iv) the mixed  
86 mechanism, i.e., flow pathways are connected with both newly created and  
87 pre-existing fractures (Norbeck et al., 2016; Lei et al., 2021). Since different  
88 communities tend to rely on a different stimulation concept. For example,  
89 the opening mode is commonly the preferred stimulation in oil/gas industry,  
90 while hydro-shearing is widely used in the context of Enhanced Geothermal  
91 System (EGS). Numerous field observations are also supportive of the benefit  
92 from the mixed stimulation (Albaric et al., 2014; Norbeck et al., 2018; Kri-  
93 etsch et al., 2020). Moreover, a recent study also suggests an important role  
94 of the stress transfer from hydraulic fracture opening in induced seismicity  
95 distribution (Kettlety et al., 2020).

96 In the context of the mixed stimulation strategy, there are two processes  
97 that could trigger seismicity, that is, the brittle failure of intact rocks by  
98 hydro-fracturing (HF) and the activation of pre-existing fractures. It has  
99 been evidenced that HF-induced seismicity in terms of magnitude is negligible  
100 compared to the fault shearing induced seismicity (Zoback, 2010; Lei et al.,  
101 2021). Hence, many studies only focus on the shear slip of natural fractures in  
102 fluid injection-induced seismicity (McClure and Horne, 2011; Rutqvist et al.,  
103 2013; Yoon et al., 2017).

104 In this study, we aim at investigating fault slip behavior during active  
105 fluid injection and after shut-in. We develop a fully hydro-mechanical cou-  
106 pling model for a fractured porous rock while considering the interaction  
107 between existing faults and the hydraulic fractures. In doing so, we consider  
108 only a single path for the stimulated fracture thereby being able to better  
109 control the model behavior. In section 2, basic governing equations are de-  
110 scribed. Section 3 introduces the model setup for the simulations, which  
111 is followed by results with parametric studies on the permeability of frac-  
112 ture damage zone (FDZ), the fault friction coefficient, fault orientation, as  
113 well as different injection scenarios. Further discussion and main conclusions  
114 are given in section 4 and section 5, respectively. A validation of hydraulic  
115 fracture propagation is also presented in the end.

## 116 **2. A coupled hydro-mechanical cohesive zone model**

117 Generally, when involving hydraulic fracturing, there are four physical  
118 processes to be considered, i.e., porous rock mass deformation, pore fluid  
119 flow, fracture fluid flow and fracture propagation (Carrier and Granet, 2012).

120 For problems which involve interactions with pre-existing faults, the fault slip  
 121 should also be defined (Chen et al., 2017; Li et al., 2017).

## 122 2.1 Porous media deformation

123 Under isothermal conditions, rock mass is considered as an isotropic,  
 124 poroelastic material. Assuming small strains, the poro-elastic constitutive  
 125 relation is expressed as (Coussy, 2004):

$$\sigma_{ij} - \sigma_{ij,0} = 2G\varepsilon_{ij} + \left(K - \frac{2}{3}G\right)\epsilon\delta_{ij} - b(p - p_0)\delta_{ij} \quad (1)$$

126 where  $\sigma_{ij}$  and  $\varepsilon_{ij}$  are the total stress and strain;  $\epsilon$  the volumetric strain;  $p$   
 127 the pore pressure;  $G$  and  $K$  are the dry elastic shear and bulk moduli, and  
 128  $b$  the Biot's coefficient. The subscript '0' represents the initial state of each  
 129 variable.

130 Eq. (1) in terms of effective stress can be simplified to:

$$\sigma'_{ij} - \sigma'_{ij,0} = 2G\varepsilon_{ij} + \left(K - \frac{2}{3}G\right)\epsilon\delta_{ij} \quad (2)$$

131 Following Biot's theory (Biot, 1941), the effective stresses tensor defined  
 132 for fully saturated media as:

$$\sigma'_{ij} = \sigma_{ij} - bp\delta_{ij} \quad (3)$$

## 133 2.2 Pore fluid flow

134 It is assumed that fluid flows through an interconnected pore network  
 135 following Darcy's law:

$$q = -\frac{k}{\eta}\nabla p \quad (4)$$

136 where  $q$  is the Darcy's velocity,  $\eta$  is the pore fluid dynamic viscosity, and  $k$   
 137 is the permeability.

138 The continuity flow equation for the fluid within the pores is given by:

$$\frac{1}{M_b} \frac{\partial p}{\partial t} + b \frac{\partial \epsilon}{\partial t} + \nabla \cdot q = 0 \quad (5)$$

139 where  $M_b$  is Biot's modulus defined by:

$$\frac{1}{M_b} = \frac{\phi_0}{K_f} + \frac{b - \phi_0}{K_s} \quad (6)$$

140 where  $K_f$ ,  $K_s$  donates the pore fluid bulk modulus and the porous medium  
 141 solid grain bulk modulus, and  $\phi_0$  is the initial porosity.

142 Combining with Eq. (4) and Eq. (5), the pore fluid diffusion equation is  
 143 obtained as follows:

$$\frac{1}{M_b} \frac{\partial p}{\partial t} + b \frac{\partial \epsilon}{\partial t} = \frac{k}{\eta} \nabla^2 p \quad (7)$$

### 144 2.3 Fluid flow inside the fracture

145 Assuming Newtonian and incompressible fluid, the flow inside a fracture  
 146 can be split into a tangential flow within the fracture and a normal flow  
 147 across the fracture walls, as shown in Fig. 1.

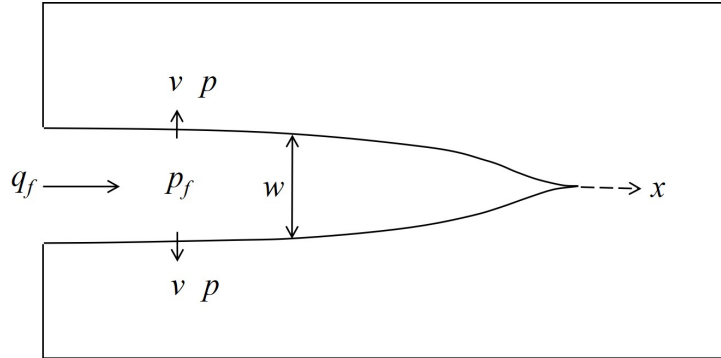


Fig. 1. Fluid flow model of the fracture



148 The tangential flow is governed by Reynold’s lubrication theory defined  
149 by the continuity equation (Detournay, 2004):

$$\frac{\partial w}{\partial t} + \frac{\partial q_f}{\partial x} + v = 0 \quad (8)$$

150 where  $w$  is the fracture aperture,  $q_f$  is the longitudinal fluid flow rate, and  $v$   
151 denotes normal flow rate leaking into the porous medium through the fracture  
152 surfaces. The latter parameter can be calculated from the difference between  
153 the fluid pressure inside the fracture  $p_f$  and the pore fluid pressure:

$$v = c(p_f - p) \quad (9)$$

154 where  $c$  is the leak-off coefficient. Eq. (9) imposes a pressure continuity  
155 between the fracture and the rock and defines a pressure-flow relationship  
156 between the cohesive element’s middle nodes and its adjacent surface nodes.  
157 In homogeneous porous reservoirs, leakoff only occurs normal from the frac-  
158 ture into the pore system. This kind of leakoff can be described by Carter’s  
159 leakoff model considering a filter-cake zone, an invaded zone, and a reservoir  
160 compaction zone (Howard and Fast, 1957; Liu et al., 2016). In such a model  
161 the leakoff coefficient as shown in Eq. (9) is pressure independent. In the  
162 case of additional natural fractures, the physics of leakoff will alter due to  
163 pressure dependent flow behavior of the fracture. In that case the leakoff  
164 coefficient becomes pressure dependent (Liu et al., 2016). In our study we  
165 only consider the first scenario, the pressure diffusion from a fracture into a  
166 porous matrix and henceforth only consider a pressure independent leakoff  
167 coefficient (Eq. 9). In addition, as leak-off coefficient and permeability in-  
168 crease, the fracture length decreases (Yao, 2012). When the permeability and  
169 the leak-off coefficient are sufficient small, the effect on the fracture length

170 will be negligible. In this work, considering the range of permeability ( $\leq$   
171  $1\text{e-}13\text{ m}^2$ ), we set the leak-off coefficient  $1\text{e-}11\text{ m}^3/\text{kPa}\cdot\text{s}$ , e.g., Yao (2012).

172 Assuming the fracture walls are parallel and smooth, the longitudinal  
173 fluid flow rate  $q_f$  is related to the pressure gradient inside the fracture as  
174 (the Poiseuille law):

$$q_f = -\frac{w^3}{12\eta} \frac{\partial p_f}{\partial x} \quad (10)$$

175 where  $q_f$  is the flow flux inside the fracture.

176 Substituting Eq. (9) and Eq. (10) into Eq. (8) yields the governing equa-  
177 tion of the fluid flow inside the fracture:

$$\frac{\partial w}{\partial t} + v = \frac{\partial}{\partial x} \left( \frac{w^3}{12\eta} \frac{\partial p_f}{\partial x} \right) \quad (11)$$

## 178 2.4 Fracture initiation and propagation

179 For hydraulic fracturing, coupled stress-pressure cohesive elements with  
180 displacement and pore pressure degrees of freedom (DOFs) are simultane-  
181 ously used. They are embedded in solid continuum elements (also with pres-  
182 sure DOF) to define a predefined crack path, such that the fracture growth  
183 is constrained to this path. Cohesive elements have been widely used to  
184 study fracture problems in rock-like materials (Zhuang et al., 2014; Saadat  
185 and Taheri, 2019). During the fracture propagation, a small fracture process  
186 zone (FPZ) is formed to capture stress concentration around the crack tip.  
187 In this study, we assume the damage initiation and evolution follow a linear  
188 traction-separation law (Fig. 2). The relation between the traction  $T$  and  
189 the separation  $\delta$  is given by (Yao, 2012):

$$T = (1 - D)K_0\delta \quad (12)$$

190 where  $D(0 \leq D \leq 1)$  is the damage variable and  $K_0$  is a penalty stiffness,  
 191 introduced to avoid total compliance of the whole model before initiation  
 192 (Turon et al., 2007).

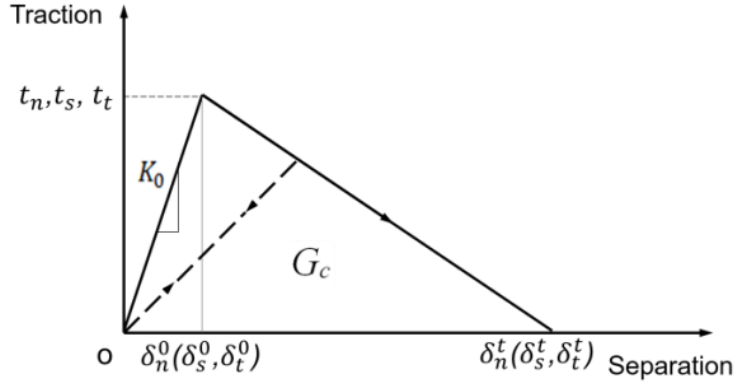


Fig. 2. Linear elastic traction-separation cohesive model

193 The total separation (i.e., fracture propagation) is depend on the fracture  
 194 energy  $G_c$  and the damage initiation is determined by the maximum nominal  
 195 stress criterion:

$$\max \left\{ \frac{\langle t_n \rangle}{t_n^0}, \frac{t_s}{t_s^0}, \frac{t_t}{t_t^0} \right\} = 1 \quad (13)$$

196 where  $t_n^0, t_s^0, t_t^0$  is the peak value of the nominal stress when the deformation  
 197 is either purely normal to the interface or purely in the first or the second  
 198 shear direction, respectively. The Macaulay bracket symbol “ $\langle \rangle$ ” signifies  
 199 that a pure compressive stress does not initiate damage.

## 200 2.5 Fault slip

201 The Coulomb friction law is used to model the shear slip behavior of fault.  
 202 Assuming the cohesion strength of the fault surface is negligible, i.e., for a  
 203 cohesion-less fault, the shear strength  $\tau_c$  is changing with the normal stress

204  $\sigma_n$  as follows:

$$\tau_c = \mu \cdot (\sigma_n - p) \quad (14)$$

205 where  $\mu$  is the coefficient of friction. Typically,  $\mu$  varies between 0.6 and 1 for  
206 intact rock, 0.3 and 0.6 or even lower for pre-existing faults (Zoback, 2010;  
207 Ellsworth, 2013; Gaucher et al., 2015). In this work,  $\mu = 0.2, 0.4$  and  $0.6$  are  
208 selected for parametric study.

209 As long as the shear stress exceeds the fault shear strength, the fault  
210 becomes unstable and slips along the fault plane. There are several causative  
211 processes responsible for the shear slip. For example, an increase in the shear  
212 stress, a reduction in the effective normal stress, or a decrease in the friction  
213 coefficient. The induced shear slip is often accompanied by the release of  
214 stored strain energy, hence induces seismicity.

### 215 **3. Model setup**

216 We consider hydraulic stimulation based on the assumption of mixed  
217 mechanism (i.e., both fracture opening and shearing). As shown in Fig. 3(a),  
218 we define two pre-existing faults F1 and F2 (blue solid line) in a 2D model.  
219 Those two faults are connected with potential hydraulic fracturing paths  
220 (blue dashed line), which are assumed to be parallel to the maximum princi-  
221 ple stress  $\sigma_1$  (Zoback, 2010). Each individual segment has a length of 10 m  
222 and both faults are oriented at a degree of  $\alpha$ , where  $\alpha$  is the angle between  
223 the maximum principal stress  $\sigma_1$  and the fault plane. All boundaries are fixed  
224 with zero displacement and initial pore pressure of the model. The injection  
225 point is located at the bottom of the model (red dot) and fluid is injected  
226 at a flow rate  $Q$ . To investigate the after shut-in effect, we intentionally set

227 the stop position between F1 and F2 (black dot). It will not exceed the half  
228 length of the segment (5 m) from F1 in all the simulations. To precisely  
229 describe the pore pressure diffusion, we set a relatively permeable zone near  
230 the faults and hydraulic paths (black dashed lines) for which we assumed  
231 a constant width (1 m). It is modeled by an increased permeability (con-  
232 sidered as an effective value averaging local micro-structural heterogeneities)  
233 than the intact rock matrix, similar to the fault damage zone (FDZ) (Evans  
234 et al., 1997; Nara et al., 2011; Mitchell and Faulkner, 2012; Hearn et al.,  
235 2018), where the fracture density is high. In addition, we also consider an  
236 exchange of fluid mass from the fractures to the permeable zone, in order to  
237 explore the impact of its permeability (linked with pressure diffusion) on the  
238 fault slip.

239 At the intersection of hydraulic fracturing path and fault, we assume that  
240 the fluid is directly diverted to the fault. This assumption is supported by  
241 previous studies which indicated that for a ratio of the initial maximum to  
242 the minimum stress larger than 1, and for a friction coefficient smaller than  
243 0.65 and fracture orientation lower than  $45^\circ$ , a hydraulic fracture will be  
244 diverted into the pre-existing fault (Gu et al., 2012).

245 In addition, the porous medium is assumed to be fully saturated. The  
246 simulations are performed in Abaqus package. All parameters used are listed  
247 in Tab. 1.

#### 248 **4. Results and analysis**

249 Fig. 4 shows the fluid pressure distribution at different time, and Fig. 5  
250 presents the fluid pressure evolution at the injection point and the center of

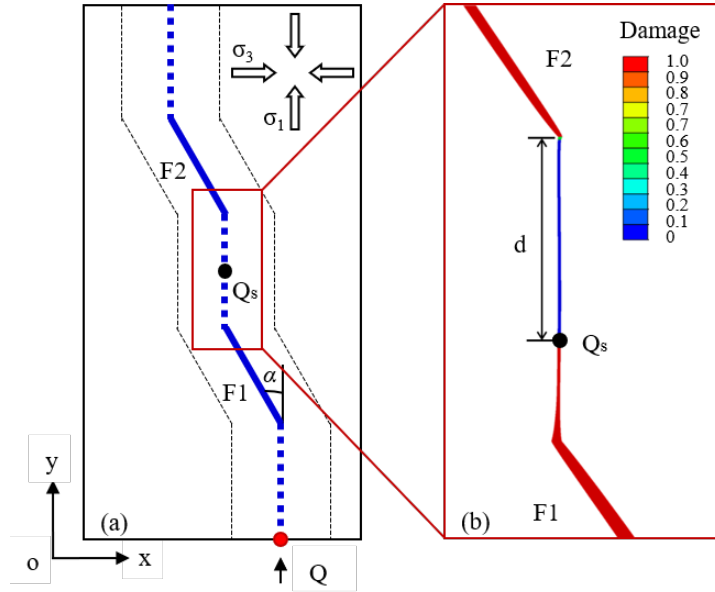


Fig. 3. (a) Geometry of the conceptual model. The red dot represents the injection point. The blue dashed line and blue solid line indicate hydraulic fracturing paths and pre-existing faults, respectively. Each segment is 10 meters long. The two parallel black dashed lines denote permeable fault damage zone. (b) Schematic diagram of induced fault slip during and after injection. The point  $Q_s$  represents the stop injection position.  $d$  is the quiescence space between  $Q_s$  and the fault F2. The red and blue color denotes the damage variable  $D = 1$  and  $D = 0$ , which indicates fully damage and zero damage respectively.

Table 1. Initial input material properties

| Property                | Symbol               | Value   | Unit                            | Notes                |
|-------------------------|----------------------|---------|---------------------------------|----------------------|
| Young's modulus         | $E$                  | 37.5    | GPa                             | (Meyer et al., 2017) |
| Poisson ratio           | $\nu$                | 0.25    | -                               | (Meyer et al., 2017) |
| Porosity                | $\phi$               | 0.01    | -                               | -                    |
| Rock permeability       | $k$                  | 1.0e-16 | m <sup>2</sup>                  | -                    |
| Permeability near fault | $k_f$                | 1.0e-15 | m <sup>2</sup>                  | -                    |
| Fracture Energy         | $G_c$                | 80      | Pa·m                            | -                    |
| Tensile strength        | $T_c$                | 2       | MPa                             | -                    |
| Penalty stiffness       | $K_0$                | 800     | GPa/m                           | (Turon et al., 2007) |
| Biot's coefficient      | $b$                  | 1.0     | -                               | -                    |
| Friction coefficient    | $\mu_1, \mu_2$       | 0.2     | -                               | -                    |
| Fault orientation       | $\alpha_1, \alpha_2$ | 30      | °                               | -                    |
| Initial aperture        | $w$                  | 0.4     | mm                              | (Meyer et al., 2017) |
| Fluid viscosity         | $\eta$               | 0.001   | Pa·s                            | water                |
| Leak-off coefficient    | $c$                  | 1.0e-11 | m <sup>3</sup> /kPa·s           | (Yao, 2012)          |
| Saturated degree        | $s$                  | 100     | %                               | -                    |
| Initial maximum stress  | $\sigma_1$           | 36      | MPa                             | (Meyer et al., 2017) |
| Initial minimum stress  | $\sigma_3$           | 29      | MPa                             | (Meyer et al., 2017) |
| Initial pore pressure   | $p_0$                | 23.7    | MPa                             | (Meyer et al., 2017) |
| Injection rate          | $Q$                  | 0.001   | m <sup>3</sup> ·s <sup>-1</sup> | -                    |
| Injection time          | $t_i$                | 160     | s                               | -                    |
| Shut-in time            | $t_s$                | 600     | s                               | -                    |

251 F1, F2. The fault F1 is activated at 38.1 s while F2 is triggered at 520.1 s  
252 (i.e., 360.1 s after shut-in). This can be identified by the damage variable  
253 (Fig. 3b).

254 At the beginning, due to high-pressure fluid stimulation, the injection  
255 pressure rises to approximately 67 MPa from an initial value 23.7 MPa in a  
256 very short time ( $\approx 2.7$  s). Due to this drastic pressure change, the induced  
257 tensile stress is sufficient to overcome the rock tensile strength. As the hy-  
258 draulic fracture propagates, the fluid pressure tends to drop to a stable level.  
259 Meanwhile, the fluid pressure at the center of F1 and F2 increases, since  
260 the high-pressure fluid inside the hydraulic fracture leaks into the surround-  
261 ing porous rock mass and then diffuses all around. At 38.1 s (point A in  
262 Fig. 5), the injected water diverts to F1, which lowers the injected pressure  
263 and forces the fluid pressure of F1 to increase. This is accompanied by a  
264 shear slip along F1 as its shear strength is overcome by the high pressure  
265 (see Fig. 8a). Meanwhile, the pressure in the center of F2 witnesses a slight  
266 jump due to poro-elastic effect. Immediately afterwards, the pressure within  
267 F1 also decreases due to the generation of a new hydraulic fracture from  
268 the end of F1. This pressure drop in regions near fracture intersections is  
269 a common feature which has been already observed by other authors, e.g.,  
270 Piris et al. (2018). From this time onward, the fluid pressures at injection  
271 point and F1 almost remain a same level with a tiny difference owing to the  
272 fluid flowing into the matrix. After 160 s of injection (point B in Fig. 5),  
273 the pumping stops and the fluid pressure starts to decrease. Pore pressure  
274 diffusion away from the pressurized hydraulic fracture can indeed be clearly  
275 observed (Fig. 6a). After approximately 360.1 s of termination of the injec-



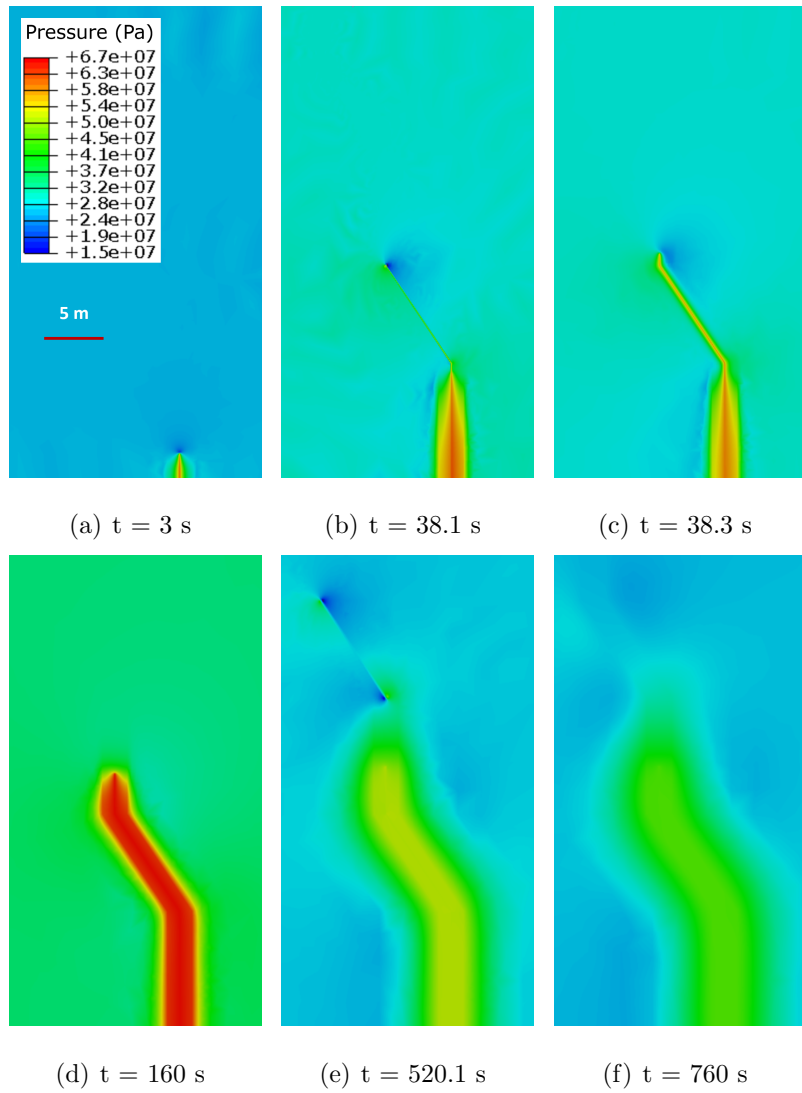


Fig. 4. Pore pressure distribution during injection and after termination. (a) onset of the injection; (b) F1 activation; (c) the second hydraulic fracture initiation; (d) stop injection; (e) F2 activation; (f) pore pressure diffusion in the porous rock matrix

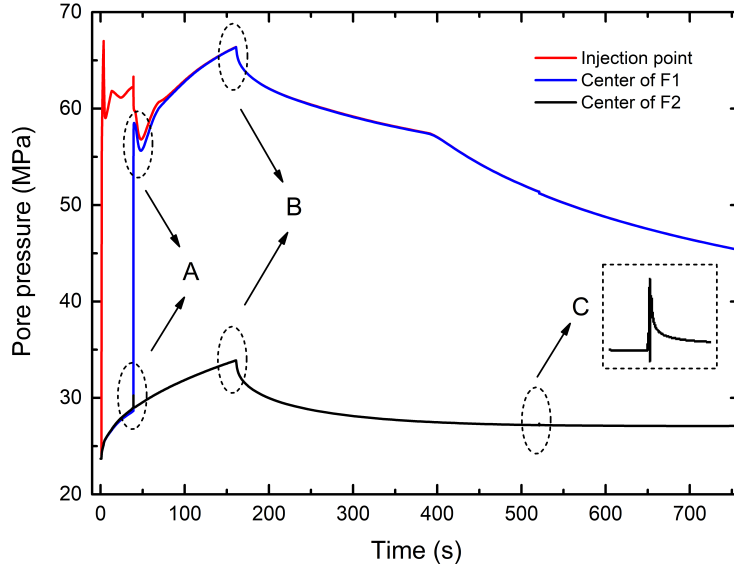


Fig. 5. Pore pressure evolution at the injection point and the center of fault F1 and F2

276 tion, the pressure perturbation and the corresponding stress change promote  
 277 instability along the fault. As the fault slips, a compressional zone and a  
 278 dilation zone emerge around the fault tip (Fig. 6). High pressure and stress  
 279 in the compressional zone and low pressure and stress in the dilation zone  
 280 are observed, respectively. This leads to only a minor increase in pressure at  
 281 the F2 center (point C in Fig. 5), but to a rather significant increase at Node  
 282 2 within the compressional zone (point C in Fig. 7). See also Fig. 6 for their  
 283 relative locations. This poro-elastic stressing mechanism is similar to the  
 284 one described by injection into a single fracture embedded in a poro-elastic  
 285 medium (Lei et al., 2021), and the combined induced fault slip mechanism  
 286 (i.e., interaction between delayed pressure diffusion and poro-elasticity) dur-  
 287 ing shut-in is in agreement with the results from previous investigation, e.g.,  
 288 Chang et al. (2018).

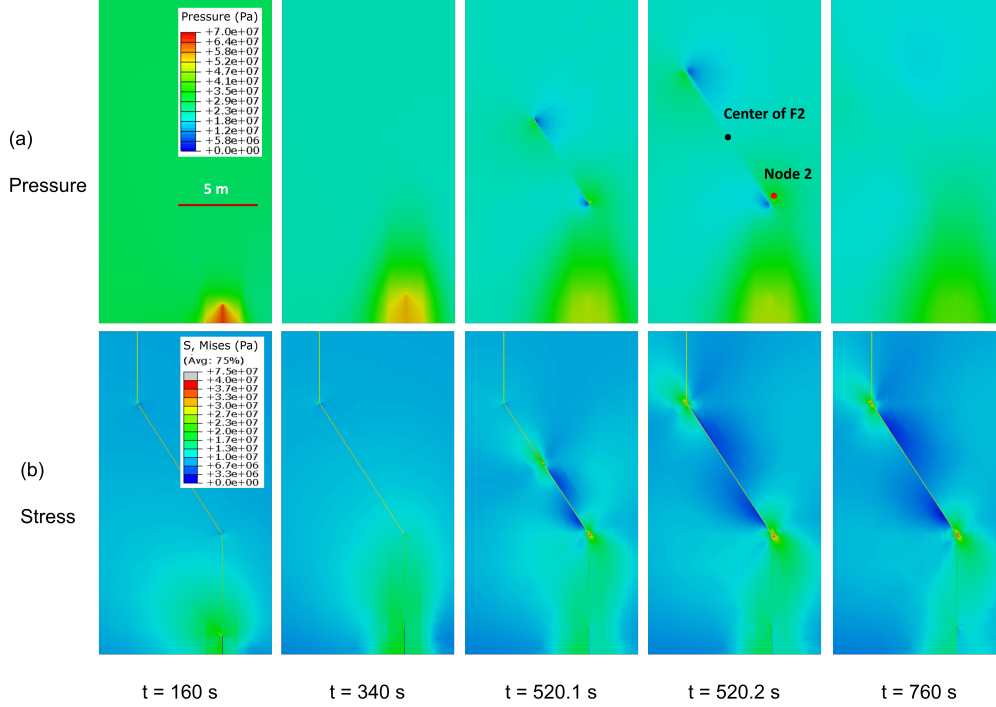


Fig. 6. Evolution of (a) pressure and (b) stress of F2 during shut-in stage

289 In fact, the sudden elevated fluid pressure, either owing to direct injection  
 290 in F1 or pressure diffusion/poro-elasticity for F2, counteracting the normal  
 291 stress and inducing dynamic slip of the fault, which correlates to potential  
 292 micro-seismic events. The evolution of slip and slip rate of F1 and F2 over  
 293 time is presented in Fig. 8. The characterization of displacement jump and  
 294 slip rate rise is similar to an unloading experiment of a sawcut fracture (Ji  
 295 et al., 2019). It can also be seen that in most of time the slip rates of F1  
 296 and F2 are close to zero, indicating an aseismic behavior. The seismic and  
 297 aseismic slip is distinguished with a slip velocity threshold 5 mm/s (McClure  
 298 and Horne, 2011; Cappa et al., 2018). In the following, the seismic slip and

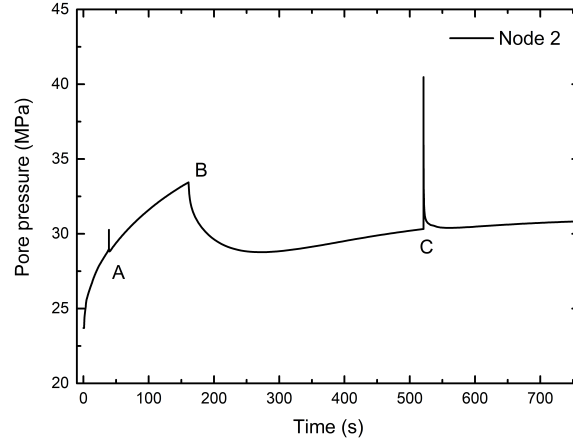


Fig. 7. Pore pressure evolution of Node 2 in the compressional zone

299 the associated average slip rate are calculated for each case.

#### 300 4.1 Permeability of the fault damage zone

301 Pore pressure diffusion in a fractured porous medium is of central impor-  
 302 tance in fluid injection in faulted reservoirs (Chang and Segall, 2016; Shapiro  
 303 et al., 1999). The core controlling parameter is the hydraulic diffusivity,  
 304 which is related to the permeability (Deng et al., 2021; Shapiro et al., 1999).  
 305 In order to investigate the impact of the hydraulic pressure diffusion on the  
 306 fault slip, we carry out a systematic analysis on the role of the fault dam-  
 307 age zone (FDZ) permeability by varying its value within three steps, that is,  
 308  $k_{f1} = 1e-15 \text{ m}^2$ ,  $k_{f2} = 5e-15 \text{ m}^2$  and  $k_{f3} = 1e-14 \text{ m}^2$ . We perform several  
 309 simulations at each permeability by altering the injection duration, in order  
 310 to capture the activation of F2 after shut-in. The corresponding results are  
 311 summarized in Tab. 2.

Table 2. Summary of key parameters and results with different permeability within the damage zone

| <b>Case*</b> | <b>Injection time (s)</b> | <b>Permeability of FDZ (m<sup>2</sup>)</b> | <b>Slip onset of F1 (s)</b> | <b>Slip onset of F2 (s)**</b> |
|--------------|---------------------------|--|-----------------------------|-------------------------------|
| A1           | 150                       | 1.0e-15                                    | 38.12                       | -                             |
| A2           | 160                       | 1.0e-15                                    | 38.12                       | 360.1                         |
| A3           | 165                       | 1.0e-15                                    | 38.12                       | 188.1                         |
| A4           | 170                       | 1.0e-15                                    | 38.12                       | 74.5                          |
| A5           | 120                       | 5.0e-15                                    | 42.01                       | -                             |
| A6           | 130                       | 5.0e-15                                    | 42.01                       | 199.4                         |
| A7           | 140                       | 5.0e-15                                    | 42.01                       | 86.0                          |
| A8           | 160                       | 5.0e-15                                    | 42.01                       | 34.7                          |
| A9           | 100                       | 1.0e-14                                    | 35.83/47.81                 | -                             |
| A10          | 110                       | 1.0e-14                                    | 35.83/47.81                 | 141.4                         |
| A11          | 130                       | 1.0e-14                                    | 35.83/47.81                 | 25.2                          |
| A12          | 160                       | 1.0e-14                                    | 35.83/47.81                 | 150.8 (in)                    |

\* all cases have fault orientation  $\alpha = 30^\circ$ , friction coefficient  $\mu_1 = \mu_2 = 0.2$ , injection rate  $Q = 0.001 \text{ m}^3/\text{s}$ ;

\*\* the slip time of F2 specifies the time after termination; F2 slip during injection is marked as '(in)'. All the same below.

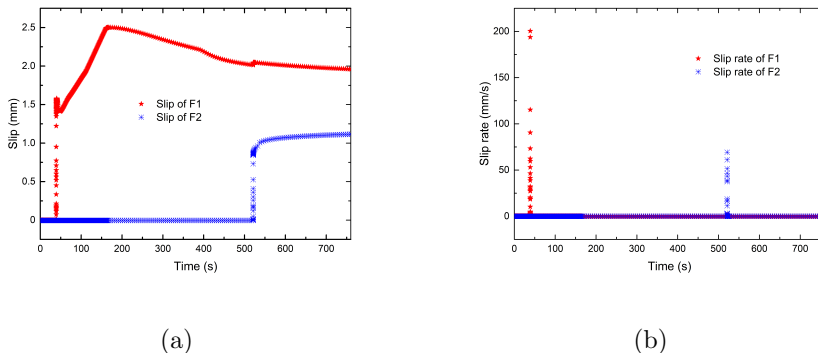


Fig. 8. Evolution of (a) total slip and (b) slip rate of F1 and F2 over time

312 It is worth noting that the permeability of FDZ is higher than the matrix  
 313 permeability ( $1e-16 \text{ m}^2$ ) hence allows faster pore pressure diffusion in the  
 314 damage zone. The time at which the hydraulic fracture intersects F1 scales  
 315 with the permeability, since higher permeability values promote faster diffu-  
 316 sion and therefore a slower fracture propagation (Carrier and Granet, 2012).  
 317 Meanwhile, due to fluid leak-off from the hydraulic fracture into the ma-  
 318 trix, the pressure front propagates faster than the hydraulic fracturing front  
 319 (Fig. 9). Here, the pressure front is defined as the pressure contour above  
 320 the initial pore pressure. We noticed that when the matrix permeability is  
 321 relatively low (case A2 and A8), the difference in the timing between the two  
 322 propagating fronts is small (Fig. 9a and Fig. 9b). When the permeability is  
 323 high (case A12), the pressure front significantly exceeds the fracturing front  
 324 (Fig. 9c). If the leak-off is ignored (e.g., the KGD problem described in the  
 325 Appendix A), the pressure front and the fracturing front coincide (Fig. 9d).

326 Therefore, the fault F1 will be overpressurized before a hydraulic connec-  
 327 tion with the injection source is reached. This over-pressure combined with

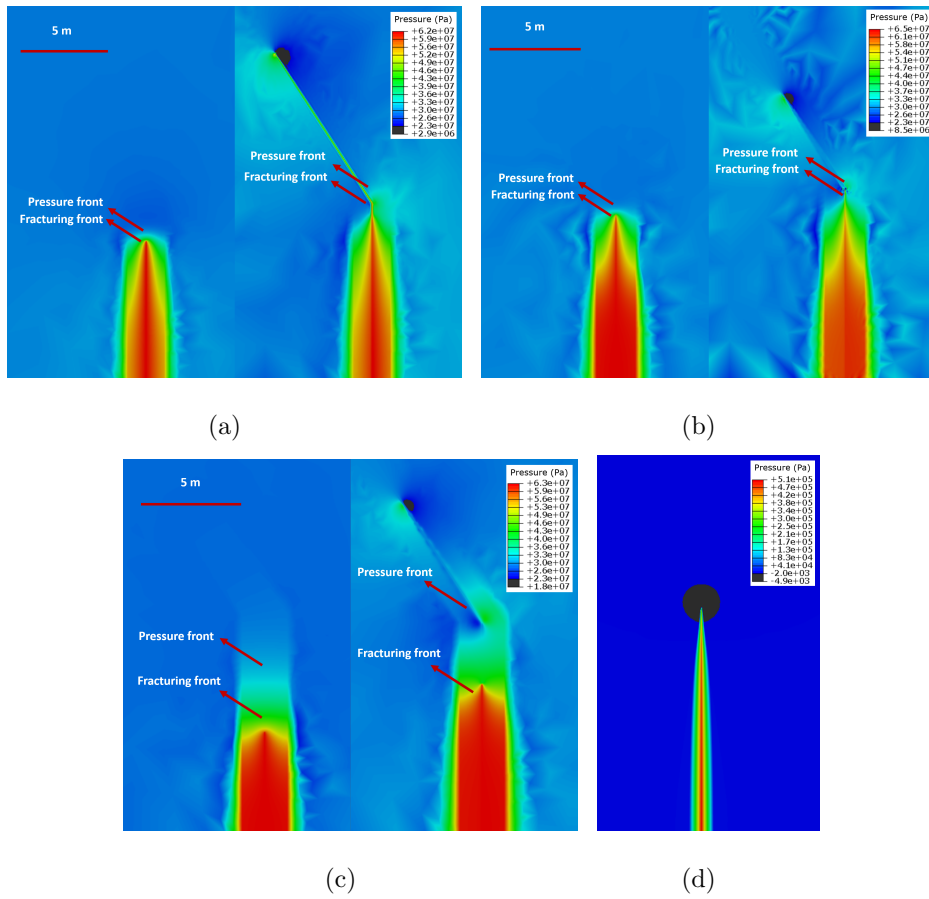


Fig. 9. Hydraulic fracturing front and pressure front propagation. (a) case A2; (b) case A8; (c) case A12; (d) case with no leak-off

328 poro-elastic stressing results in a reduction of the effective normal stress  
329 and induces slip along F1 because the induced shear stress exceeds its shear  
330 strength. The time lag of the over-pressurized front and fracturing front for  
331 cases A2 and A8 is very small ( $< 0.1$  s) such that the sliding looks more  
332 continuous. However, for case A12 with a higher FDZ permeability, this  
333 time lag becomes obvious ( $\sim 12$  s), and F1 undergoes two distinct slips due  
334 to over-pressurization and hydraulic shearing, respectively. During the first  
335 slip, the total shear slip and slip rate are smaller than those obtained for case  
336 A2 and A8, since the pressure perturbation is lower. During the second slip,  
337 there is mainly aseismic slip and this is because most of the accumulated  
338 strain energy has been released during the first slip. As a result, the slip and  
339 slip rate of F1 exhibit an obvious downward trend as permeability increases  
340 (Fig. 10a).

341 For each tested value for the FDZ permeability, we observed that F2 is  
342 activated by the pressure diffusion and poro-elasticity though the activation  
343 time differs for each case. A higher permeability requires less fluid injection,  
344 i.e., 150 - 160 s for  $k_{f1} = 1\text{e-}15$  m<sup>2</sup>, 120 - 130 s for  $k_{f2} = 5\text{e-}15$  m<sup>2</sup>, and  
345 only 100 - 110 s for  $k_{f3} = 1\text{e-}14$  m<sup>2</sup>. When the injection time is identical,  
346 the higher the permeability, the shorter the time lag for F2 reactivation. For  
347 example, with an injection duration of 160 s, F2 has a quiescence of 360.1 s  
348 and 34.7 s after shut-in for case A2 and case A8, whereas it is even activated  
349 during the injection for case A12. The permeability has a limited influence  
350 on magnitude of resolved slip and its rate of F2, which are around 0.8 mm  
351 and 35 mm/s (Fig. 10b), respectively. They are slightly increased with more  
352 fluid injection at each permeability.



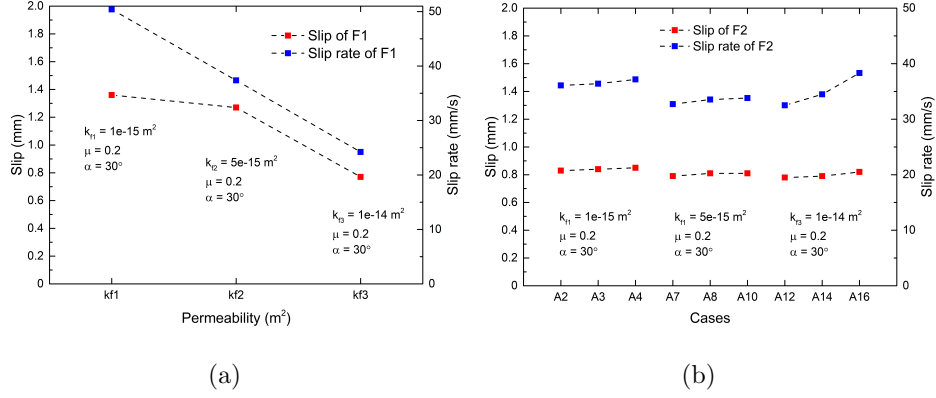


Fig. 10. Seismic slip and slip rate of (a) F1 and (b) F2 with different permeability in the damage zone

## 353 4.2 Friction coefficient

354 The effect of the friction coefficient on fault slip behavior due to direct  
 355 injection can be seen from Fig. 11(a), corresponding to cases A2, B1 and B2  
 356 in Tab. 3. Triggering by direct fluid injection, faults with a higher friction  
 357 coefficient tend to display a higher level of slip and higher slip rates. As  
 358 stated by Ngo et al. (2019), this is because more accumulated energy are  
 359 required to activate faults with higher friction coefficient, and accordingly  
 360 more energy is released during slip. In addition, unlike faults with a smaller  
 361 friction coefficient, which are more likely to be activated by pressure diffusion  
 362 and poro-elastic stressing before hydraulic shearing, the faults with higher  
 363 friction coefficient tend to slip only during hydraulic shearing and therefore  
 364 more violently.

365 As for the shut-in stage, because F2 cannot be activated with permeability  
 366  $k_f = 1e-15 \text{ m}^2$  in case B1, we keep the friction coefficient of F1 constant  
 367 as  $\mu_1 = 0.2$  and set case A12 as the base case ( $k_f = 1e-14 \text{ m}^2$ ). When

368 the friction coefficient of F2 is 0.4, F2 activation can be observed either by  
 369 increasing injection duration to 180 s (case B4) or permeability to  $1\text{e-}13\text{ m}^2$   
 370 (case B5). For  $\mu_2 = 0.6$ , F2 cannot be triggered unless these two parameters  
 371 are simultaneously increased (case B7). These illustrate that a higher friction  
 372 coefficient hinders fault reactivation. However, once F2 slips, higher slip and  
 373 slip rate are observed when the friction coefficient is larger (Fig. 11(b)),  
 374 similar to the slip behavior observed during the fluid injection phase.

Table 3. Summary of key parameters and results with different friction coefficient

| Case* | Injection time (s) | $k_f$ ( $\text{m}^2$ ) | $\mu_1$ | $\mu_2$ | Slip onset of F1 (s) | Slip onset of F2 (s) |
|-------|--------------------|------------------------|---------|---------|----------------------|----------------------|
| A2    | 160                | 1.0e-15                | 0.2     | 0.2     | 38.12                | 360.1                |
| B1    | 160                | 1.0e-15                | 0.4     | 0.4     | 38.12                | -                    |
| B2    | 160                | 1.0e-15                | 0.6     | 0.6     | 38.12                | -                    |
| A12   | 160                | 1.0e-14                | 0.2     | 0.2     | 35.83                | 150.8 (in)           |
| B3    | 170                | 1.0e-14                | 0.2     | 0.4     | 35.83                | -                    |
| B4    | 180                | 1.0e-14                | 0.2     | 0.4     | 35.83                | 75.7                 |
| B5    | 160                | 1.0e-13                | 0.2     | 0.4     | 25.62                | 145.9 (in)           |
| B6    | 175                | 1.0e-13                | 0.2     | 0.6     | 25.62                | -                    |
| B7    | 180                | 1.0e-13                | 0.2     | 0.6     | 25.62                | 10.2                 |

\* all cases have fault orientation  $\alpha = 30^\circ$ ,  $\mu_1 = 0.2$ , injection rate  $Q = 0.001\text{ m}^3/\text{s}$ ;

### 375 4.3 Fault orientation

376 On the basis of case A2, we conduct additional simulations where we  
 377 varied the fault orientation, by changing the fault angle  $\alpha$  (tested value are

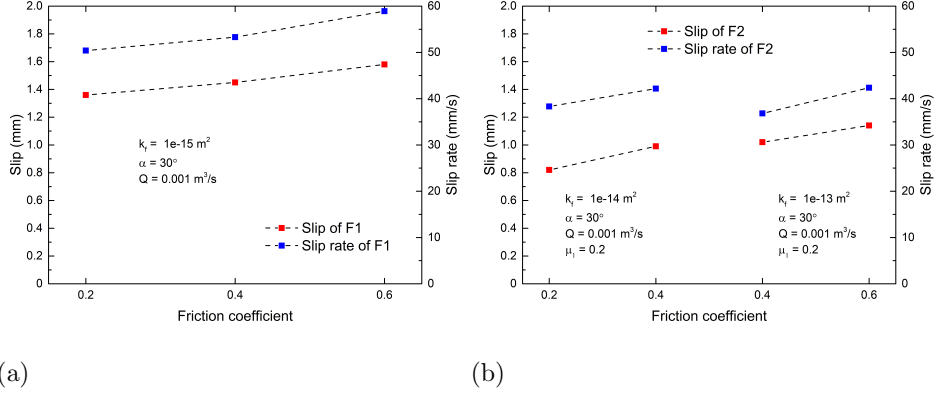


Fig. 11. Seismic slip and slip rate of (a) F1 and (b) F2 with different friction coefficient

378 45°, 20° and 10°, see Tab. 4).

379 During the fluid injection stage, the hydraulic connection of the injection  
 380 well-bore and the fault F1 occurs at 40.68 s, 39.48 s, 38.12 s, and 35.83 s when  
 381 the fault angle increases from 10° to 45°, suggesting that a smaller fault dip  
 382 tends to hinder hydraulic fracture propagation. We infer that this is because  
 383 the pre-existing fault modifies local stress distributions and the latter depends  
 384 primarily on the fault orientation. In addition, as the fault dip decreases,  
 385 the triggered slip and slip rate decrease (Fig. 12(a)), in particular, when the  
 386 fault angle is 10° (case C4), the slip exhibits mainly aseismic behavior and  
 387 the averaged slip rate is only about 2.3 mm/s.

388 During the shut-in stage, except case A2, only case C1 with  $\alpha = 45^\circ$   
 389 induces F2 activation at 85.7 s after termination in comparison with 360.1  
 390 s in case A2. For the 20° model, the shut-in effect of F2 appears when the  
 391 permeability of FDZ is enhanced from  $k_{f1} = 1e-15 \text{ m}^2$  to  $k_{f3} = 1e-14 \text{ m}^2$   
 392 (case C3). For the 10° model, F2 can be activated not only with even a  
 393 higher FDZ permeability ( $1e-13 \text{ m}^2$ ), but a higher injection rate  $1.6 \text{ m}^3/\text{s}$  in

394 case C3 (we will show that a higher injection rate is more likely to trigger  
 395 shut-in slip in the next section). The results demonstrate that a higher fault  
 396 orientation is more sensitive to F2 reactivation after shut-in. Furthermore,  
 397 it tends to induce a larger shear slippage with a higher slip rate (Fig. 12(b)).

Table 4. Summary of key parameters and results with different fault angle

| <b>Case*</b> | <b>Injection<br/>time (s)</b> | <b><math>k_f</math> (m<sup>2</sup>)</b> | <b><math>\alpha</math><br/>(°)</b> | <b>Slip onset<br/>of F1 (s)</b> | <b>Slip onset<br/>of F2 (s)</b> |
|--------------|-------------------------------|---|------------------------------------|---------------------------------|---------------------------------|
| A2           | 160                           | 1.0e-15                                 | 30                                 | 38.12                           | 360.1                           |
| C1           | 160                           | 1.0e-15                                 | 45                                 | 35.83                           | 85.7                            |
| C2           | 160                           | 1.0e-15                                 | 20                                 | 39.48                           | -                               |
| C3           | 160                           | 1.0e-14                                 | 20                                 | 40.16                           | 42.2                            |
| C4           | 160                           | 1.0e-15                                 | 10                                 | 40.68                           | -                               |
| C5           | 100                           | 1.0e-13                                 | 10                                 | 35.07                           | 4.0                             |

\* all cases have  $\mu_1 = \mu_2 = 0.2$ , injection rate  $Q = 0.001 \text{ m}^3/\text{s}$  except for case C7, which is  $0.0016 \text{ m}^3/\text{s}$ .

#### 398 4.4 Injection scheme

399 In this section, we investigate the effect of injection scheme, by considering  
 400 case A2 as the reference case (Tab. 5).

401 In a first step, we change the injection rate to  $0.0016 \text{ m}^3/\text{s}$ ,  $0.0008 \text{ m}^3/\text{s}$   
 402 and  $0.0005 \text{ m}^3/\text{s}$ , corresponding cases E1, E2 and E3 (Fig. 13a), respectively.  
 403 Worth noting is that we adjust the duration of the injection as to maintain  
 404 the same injection volume for all experiments. As expected, lowering the  
 405 injection rate extends the time to reactivate F1. When  $Q = 0.0016$ ,  $0.001$   
 406 and  $0.0008 \text{ m}^3/\text{s}$ , F2 can be reactivated but with a longer delay at 97.7 s,

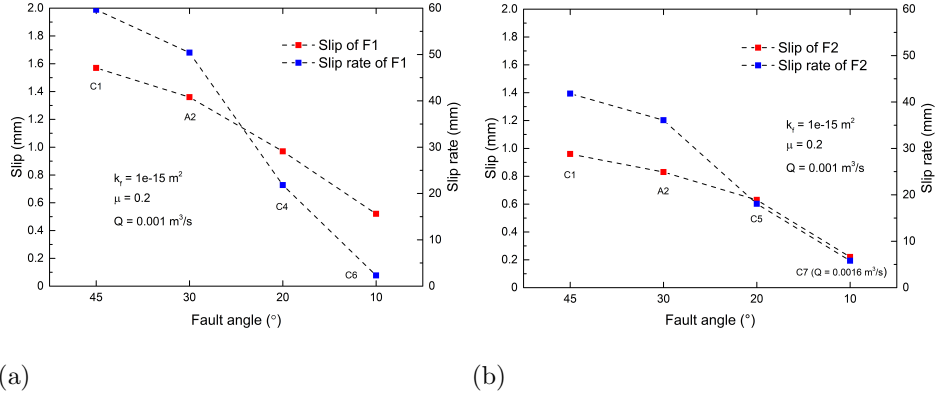


Fig. 12. Seismic slip and slip rate of (a) F1 and (b) F2 with different fault angle

407 360.1 s and 410 s after shut-in, respectively. No slip of F2 is observed when  
 408 the injection rate further reduces to  $0.0005 \text{ m}^3/\text{s}$ . Either during injection or  
 409 after shut-in, the injection rate has only a limited impact on the total seismic  
 410 slip, though fault slip rates decrease with decreasing injection rates (Fig. 14),  
 411 which results in a more stable energy release mode.

412 In a second stage, we keep the injection rate as constant ( $0.001 \text{ m}^3/\text{s}$ ), but  
 413 we change the injection protocol. We consider a step-wise injection schedule  
 414 (a period of constant injection followed by a pause) by maintaining the same  
 415 total volume of fluid injected (Fig. 13b).

416 In case E4, the stimulation is divided evenly into 4 injections and 3 pauses  
 417 (i.e., a cycling stimulation), each injection/pulse has a duration of 40 s.  
 418 Since F1 reactivation occurs at  $38.12 \text{ s} < 40 \text{ s}$  in case A2, this setting will  
 419 not change the response of F1 during injection. However, the relaxation of  
 420 stimulation during the injection favours pressure relaxation, which prevents  
 421 the reactivation of F2. In case E5, the first injection and suspending time  
 422 in case E4 are changed to 30 s and 50 s, respectively. In this case, F1 is

423 activated during the first pause (47.83 s) due to pressure diffusion and poro-  
424 elastic stressing, while mainly hydraulic shearing occurs during the second  
425 injection (80.27 s). Compared to case E4, not only F2 reactivation after  
426 shut-in is prevented in case E5, but the injection-induced slip and slip rate  
427 of F1 are significantly reduced owing to the double slip effect, i.e., 1.36 mm  
428 and 50.4 mm/s for case E4 vs. 0.75/0.18 mm and 26.97/25.95 mm/s for case  
429 E5. It is equivalent to artificially extend the interval between the pressure  
430 diffusion and hydraulic shearing, producing a longer and more stable energy  
431 release.

Table 5. Summary of key parameters and results with different injection schemes

| Case* | Injection time (s) | Injection rate (m <sup>3</sup> /s) | Slip onset of F1 (s) | Slip onset of F2 (s) |
|-------|--------------------|------------------------------------|----------------------|----------------------|
| A2    | 160                | 0.001                              | 38.12                | 360.1                |
| E1    | 100                | 0.0016                             | 21.85                | 97.7                 |
| E2    | 200                | 0.0008                             | 47.24                | 410.0                |
| E3    | 320                | 0.0005                             | 73.17                | -                    |
| E4    | 40×4               | 0.001                              | 38.12                | -                    |
| E5    | 30+50+40×2         | 0.001                              | 47.83/80.27          | -                    |

\* all cases have  $k_f = 1\text{e-}15 \text{ m}^2$ ,  $\mu_1 = \mu_2 = 0.2$ , fault orientation  $\alpha = 30^\circ$ .

## 432 5. Discussion

### 433 5.1 Comparison with earthquake fault scaling relations

434 It is well known that unstable fault slip is accompanied by a cluster of  
435 induced seismic events (Zoback, 2010; Ellsworth, 2013). To quantify their

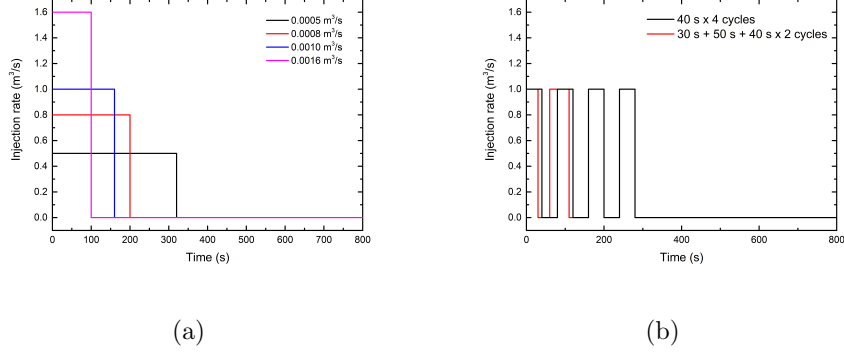


Fig. 13. Injection scenarios with a constant injection volume: (a) constant injection rate and (b) cyclic injection rate

436 strength, Aki (1966) first defined the scalar seismic moment  $M_0$  as:

$$M_0 = G\bar{d}A \quad (15)$$

437 where  $G$  is the shear modulus,  $\bar{d}$  and  $A$  denote the fault shear displacement  
438 and fault rupture area, respectively.

439 The moment magnitude  $M_w$  can be then computed by assuming a GR  
440 statistics as (Hanks and Kanamori, 1979):

$$M_w = \frac{2}{3}[\log_{10}(M_0) - 9.1] \quad (16)$$

441 where we consider a GR b-value equal to 1 in deriving Eq. (16).

442 We calculate the moment magnitude for each case based on the obtained  
443 seismic slip. Considering that the fault slip occurs during a very short time,  
444 we assume that the rupture covers the whole fault, therefore the rupture  
445 length is identical to the fault length, and we can approximate the sliding  
446 distance as the average seismic slip computed (Lei et al., 2021). For calcu-

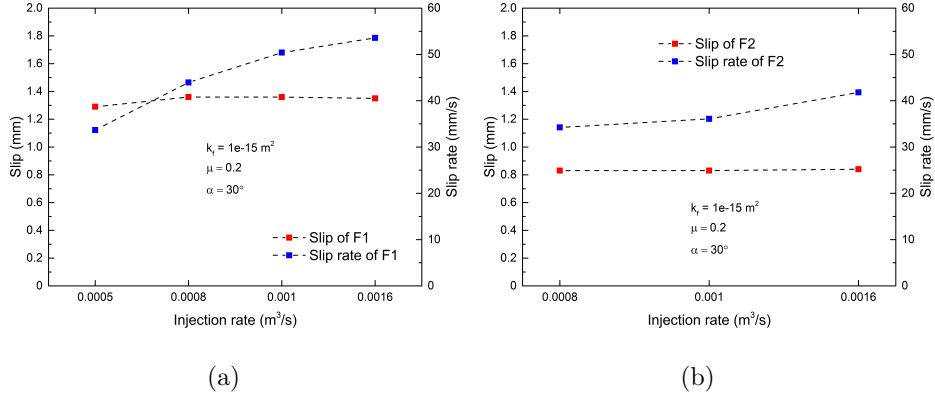


Fig. 14. Seismic slip and slip rate of (a) F1 and (b) F2 with different injection scenarios

447 lating the rupture area, we assume that the rupture width is equal to the  
 448 rupture length, which is supported by a large number of reported earthquakes  
 449 (Yoon et al., 2017).

450 We compare the results with two earthquake fault scaling relations. The  
 451 first one describes the relationship between induced magnitude, fault size,  
 452 shear slip and stress drop (Zoback and Gorelick, 2012). In our simulations  
 453 we compute a shear slip between 0.22 and 1.57 mm, corresponding to  $M_w$   
 454 from -0.39 to 0.18. The related stress drop ranges from 4.29 MPa to 19.79  
 455 MPa, suggesting a good consistency with adopted scaling laws (Fig. 15). The  
 456 second comparison relates the magnitude with the rupture area. Although  
 457 with a smaller rupture size, our results are still in good agreement with  
 458 numerous earthquakes (Fig. 16).

## 459 5.2 Comparison induced seismicity during injection and after shut-in

460 Our results show that pre-existing faults can be reactivated and exhibit  
 461 dynamic slip under certain conditions even faults and hydraulic fractures



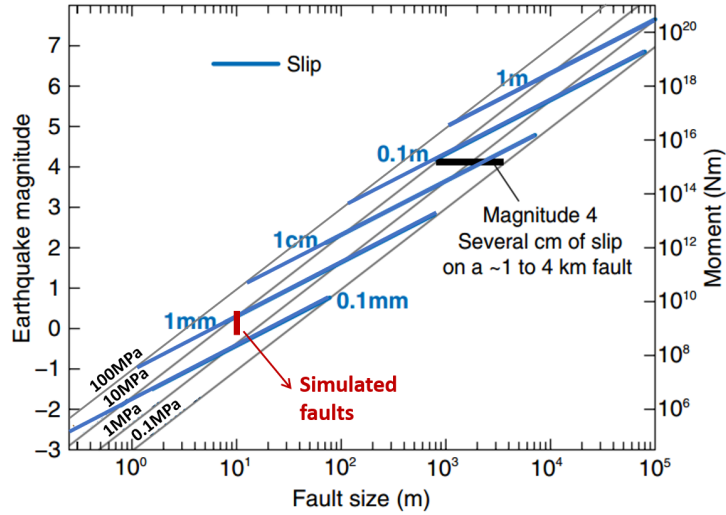


Fig. 15. Earthquake parameters scaling for fault slip, fault size, stress drop and magnitude, modified from (Zoback and Gorelick, 2012)

462 are non-hydraulically connected, illustrating that seismic events can be in-  
 463 duced during the post-injection period triggered by pore pressure diffusion  
 464 and poro-elastic stress change mechanisms. This is in agreement with field  
 465 observations as those reported in Soultz-sous-Forêt EGS site (Baisch et al.,  
 466 2010). In addition, this post-injection reactivation of fault occurs after a  
 467 period of quiescence, sometimes even exceeding twice of the injection time in  
 468 our simulations (e.g., case A2 and case E2). This delayed phenomenon has  
 469 been also observed in other EGS projects as in Rittershoffen (Lengliné et al.,  
 470 2017).

471 Most of the cases that display reactivation of F2 after shut-in we note that  
 472 induced slip and rates computed at F1 during injection are larger than those  
 473 obtained in F2 during the post injection stage. However, there are also some  
 474 cases showing an inverse trend, i.e., F2 produces more shear slip and higher

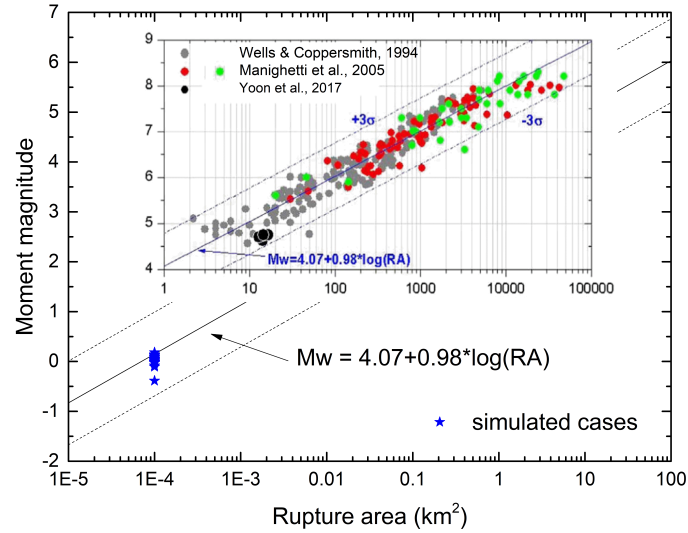


Fig. 16. Moment magnitude as a function of rupture area, modified from (Yoon et al., 2017)

475 slip rate than F1. We single out these cases and find that they generally share  
 476 similar conditions, i.e., the diffusivity (permeability) in their nearby regions  
 477 is extremely high ( $1e-14 \text{ m}^2$  or  $1e-13 \text{ m}^2$ ), e.g., cases A10 - A12, B3 - B5.  
 478 In these cases, F1 reactivation due to large pressure gradient occurs earlier  
 479 than the direct hydraulic shearing, but this pressure disturbance is smaller  
 480 compared to F2 after shut-in. Thus, the strain energy of F1 is released  
 481 more evenly than F2. The results may provide an explanation for a common  
 482 observation in the field, that is that the post injection might induce larger  
 483 magnitude earthquakes (Håring et al., 2008; Mukuhira et al., 2013). They  
 484 also shed light on mitigating the risk of fluid induced earthquake. As shown  
 485 in case E5, which displays double slip events in F1 during active injection, a

486 lower surrounding permeability ( $1e-15 \text{ m}^2$ ) significantly reduces the induced  
487 seismic slip and its slip rates. By injecting the same amount of fluid, although  
488 cases E5 and E3 both lower the slip of F1 and evade the post-activation of  
489 F2, case E5 is more efficient because it consumes less time (280 s vs. 320 s).  
490 Therefore, on the basis of our analysis, we can conclude that a soft cycling  
491 stimulation strategy might be effective in controlling fluid injection induced  
492 seismicity, as suggested by (Hofmann et al., 2018; Zang et al., 2019; Zhuang  
493 et al., 2019).

494 Our results also suggest that the permeability beyond the stimulated zone  
495 is of great importance for the shut-in phase. After shut-in, high pressure in  
496 the stimulated region diffuses to the surrounding porous matrix, and coupled  
497 to induced poro-elastic stress changes can lead to activation of F2 and induced  
498 seismicity, thereby extending the seismic region. The work of McClure (2015)  
499 showed that the fluid pressure is redistributed and pressure front progresses  
500 further after shut-in, extending the pressurized area and induces seismicity.  
501 Mukuhira et al. (2017) studied the behavior of pore pressure migration at  
502 shut-in phase in Basel and pointed out that large events tend to occur in  
503 regions with enhanced permeability. In our case, we set large permeability  
504 outside the stimulated region, causing pore pressure to migrate far field the  
505 seismic zone after termination.

### 506 5.3 The role of initial stress state

507 Our parametric study shows that there are multiple factors affecting fault  
508 slip behavior both during injection and after shut-in. For example, higher  
509 permeability reduces the seismic slip but more via double slip effect during  
510 the injection period and has little impact on the induced fault slip during

511 the shut-in stage (Fig. 10), and the soft cycle injection lowers the seismic  
512 slip rate effectively (Fig. 14). In contrast, the fault orientation seems to have  
513 the greatest influence on the fault slip. As shown in Fig. 12, when the fault  
514 angle decreases, the seismic slip and slip rate drop significantly and the faults  
515 tend to slip aseismically regardless if during injection or after shut-in. This  
516 may be related to the initial stress state of the faults. To evaluate the initial  
517 potential for fault reactivation, we calculate the slip tendency ST, which is  
518 defined as the ratio between the absolute shear stress and effective normal  
519 stress (Blöcher et al., 2018):

$$\text{ST} = \frac{|\tau|}{|\sigma'_n|} \quad (17)$$

520 The initial shear stress and effective normal stress of fault are given by  
521 (Jaeger et al., 2009):

$$\tau = \frac{\sigma_1 - \sigma_3}{2} \sin(2\alpha) \quad (18)$$

$$\sigma'_n = \frac{\sigma'_1 + \sigma'_3}{2} + \frac{\sigma'_1 - \sigma'_3}{2} \cos(2\alpha) \quad (19)$$

523 At the given initial stress state (Tab. 1), the slip tendency  $\text{ST} = 0.034$ ,  
524  $0.069$ ,  $0.096$ ,  $0.108$  for the fault angle  $\alpha = 10^\circ$ ,  $20^\circ$ ,  $30^\circ$  and  $45^\circ$ , suggesting  
525 an increasing critical condition for fault reactivation. Moreover, a larger ini-  
526 tial slip tendency leads to higher seismic slip and slip rate under the same  
527 perturbation (see Fig. 12). To further validate this hypothesis, we conduct  
528 another simulation by only reducing the minimum principal stress  $\sigma_3$  from  
529  $29$  MPa to  $24$  MPa from case A2. Accordingly, the initial slip tendency in-  
530 creases from a nominal value of  $0.096$  to  $0.155$ , approaching further to the  
531 static friction coefficient ( $0.2$ ). The results show that with only  $8.05$  s and

532 28.2 s fluid injection, F1 and F2 are both activated by coupled fluid pres-  
533 sure diffusion and poro-elastic stressing. This is consistent with the main  
534 conclusions derived in the study by Lee et al. (2019), where they analyzed  
535 induced seismicity in Pohang EGS project and found that the fault which  
536 is responsible for the earthquake, was critically stressed, susceptible to slip  
537 and very sensitive to even small perturbations. Furthermore, the slip rates of  
538 F1 and F2 also increases (mainly due to poro-elastic stressing since F1 slips  
539 aseismically when it connects the injection point at 16.87 s), indicating much  
540 stronger energy releases. This has important implications for controlling fluid  
541 injection-induced seismicity, in particular for post-injection induced seismic-  
542 ity targeting far-field faults. As suggested by (Baisch et al., 2010), post-event  
543 magnitude is predominantly affected by the fault geometry and fluid pres-  
544 sure elevation brings stress conditions close to critical values. Mukuhira et al.  
545 (2013, 2017) also demonstrated that even a minor increase in pore pressure  
546 was sufficient to initiate shear slip and trigger large events at large differential  
547 stress. Indeed, many researches even stated that the initial stress controls the  
548 nature of the fluid induced seismicity (Yoon et al., 2017; Cappa et al., 2018;  
549 Passelègue et al., 2020). This may also be one aspect to get an insight into  
550 an observation that a field area of little natural seismicity may have a lower  
551 propensity to produce felt or damaging earthquakes (Evans et al., 2012).  
552 Therefore, to mitigate the unwanted seismicity, a good prior knowledge of  
553 the crust before treatment is required.

## 554 **6. Conclusion**

555 In this study, we conducted a coupled hydraulic-mechanical numerical  
556 model to investigate the induced fault slip behavior during injection and  
557 after shut-in. It shows the capability of generating seismic slip either owing  
558 to direct hydraulic shearing or fluid pressure diffusion coupled with poro-  
559 elastic stressing when there is no connection between the hydraulic fracture  
560 and the pre-existing fault.

561 Through parametric study, we found that fault seismic slip can be at-  
562 tributed to the combined effect of multiple factors but with different em-  
563 phases. Permeability along the fracture path is of great importance not only  
564 for the after shut-in stage, but also for the fracturing process. It allows fluid  
565 pressure diffusion induced poro-elastic stress change to activate the fault  
566 before the hydraulic shearing. This averages the strain energy release and  
567 lowers the seismicity magnitude during injection, providing an explanation  
568 for the occurrence of larger earthquakes after shut-in. It also highlights the  
569 effectiveness of soft cyclic injection since the fault strain energy can be partly  
570 released during each relaxation. Moreover, although the larger friction coeffi-  
571 cient favors fault slip and the soft injection can alleviate the slip, the impact  
572 of fault orientation on the slip is more dominant. Finally, the combined ef-  
573 fect of these factors can be largely attributed to the initial slip tendency and  
574 hence the initial stress state. We confirmed that critically-stressed faults are  
575 more likely to produce larger shear slip even with only small perturbations.  
576 Our results show good consistency with some field observations and previ-  
577 ous studies, which have important implications for mitigating fluid injection  
578 induced seismicity. In the next step, the influence of fracture networks will

579 be considered.

## 580 **Declaration of Competing Interest**

581 The authors declare that they have no known competing financial inter-  
582 ests or personal relationships that could have appeared to influence the work  
583 reported in this paper.

## 584 **Acknowledgements**

585 This work was supported by the China Scholarship Council (CSC) [grant  
586 number 201808510128].

## 587 **Appendix A: Validation of the hydraulic fracture propagation**

588 For any complex numerical models involve hydraulic fracture simulation,  
589 Lecampion et al. (2018) emphasized the necessity of verification against those  
590 analytical solutions. Here the KGD (Kristianovic-Geerstma-de Klerk) model  
591 for plane strain hydraulic fracture is selected for validation (Garagash, 2006).

592 The scaling solutions for the hydraulic aperture  $w$ , the average net pres-  
593 sure  $p$ , and the fracture length  $l$  are given by (Detournay, 2004):

$$\begin{cases} w = \varepsilon(t) \cdot L(t)\Omega[x', P(t)] \\ p = \varepsilon(t) \cdot E'\Pi[x', P(t)] \\ l(t) = L(t) \cdot \gamma[P(t)] \end{cases} \quad (\text{A.1})$$

594 where  $x' = x/l(t)$  is the scaled coordinate,  $0 \leq x' \leq 1$ .  $\varepsilon(t)$ ,  $L(t)$ ,  $P(t)$   
595 denotes a small dimensionless parameter, a length scale if the same order as  
596 the fracture length  $l$ , and a dimensionless evolution parameter, respectively.

597 The hydraulic fracture propagation is controlled by either toughness-  
 598 dominated regime ( $\kappa$ -regime) or viscosity-regime ( $M$ -regime) (Carrier and  
 599 Granet, 2012). The dimensionless viscosity  $M$  and toughness  $\kappa$  is given by:

$$M = \kappa^{-4} = \mu' \frac{E'^3 Q_0}{K'^4} \quad (\text{A.2})$$

600 where  $\mu' = 12\mu$ ;  $E' = \frac{E}{1 - \nu^2}$ ;  $K' = 4 \left( \frac{2}{\pi} \right)^{1/2} K_{IC}$ .

601 The toughness scaling is most appropriate for cases when the viscosity  
 602 scaling  $M$  is small. The asymptotic solution  $\bar{F}_k(\bar{\Omega}_k, \Pi_k, \gamma_k)$  is given by:

$$\bar{F}_k = \bar{F}_{k_0} + M \bar{F}_{k_1} \quad (\text{A.3})$$

603 where  $\bar{F}_{k_0}(\bar{\Omega}_{k_0}, \Pi_{k_0}, \gamma_{k_0})$  is the zero-viscosity solution given by:

$$\begin{cases} \Omega_{k_0} = \frac{\pi^{1/3}}{2} (1 - x'^2)^{1/2} \\ \Pi_{k_0} = \frac{\pi^{1/3}}{8} \\ \gamma_{k_0} = \frac{2}{\pi^{2/3}} \end{cases} \quad (\text{A.4})$$

604 and the next term  $\bar{F}_{k_1}(\bar{\Omega}_{k_1}, \Pi_{k_1}, \gamma_{k_1})$  is:

$$\begin{cases} \Pi_{k_1} = \Pi_{k_1}^* + \Delta \Pi_{k_1} \\ \Omega_{k_1} = 4 \Pi_{k_1}^* (1 - x'^2)^{1/2} + \frac{2}{\pi} \int_0^1 f(x', x) \Delta \Pi_{k_1}(x) dx \\ \gamma_{k_1} \simeq -2.72 \end{cases} \quad (\text{A.5})$$

605 where

$$\Delta \Pi_{k_1}(x) = \frac{4}{3\pi^{2/3}} \ln(1 - x'^2) - \frac{2x' \arccos x'}{\pi^{2/3} (1 - x'^2)^{1/2}} \quad (\text{A.6})$$

606

$$f(x', x) = -\frac{4}{\pi} \ln \left| \frac{\sqrt{1 - x'^2 + \sqrt{1 - x'^2}}}{\sqrt{1 - x'^2 - \sqrt{1 - x'^2}}} \right| \quad (\text{A.7})$$



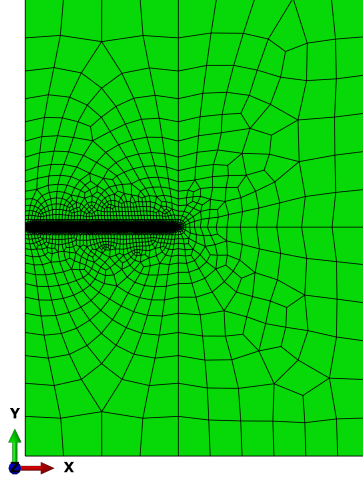


Fig. A.1. Geometry and mesh of the KGD model

607 For the toughness scaling,

$$\begin{cases} \varepsilon_k = \left( \frac{K'^4}{E'^4 Q_0 t} \right)^{1/3} \\ L_k = \left( \frac{E' Q_0 t}{K'} \right)^{2/3} \end{cases} \quad (\text{A.8})$$

608 Fig. A.1 shows the geometry and mesh used in the simulation. Here the  
 609 2D model has a dimension  $45 \text{ m} \times 60 \text{ m}$ , with a predefined hydraulic fracture  
 610 path at the middle along the  $x$ -axis, simulated by cohesive elements with pore  
 611 pressure degree of freedom. The well-bore is simplified to be a point and the  
 612 point injection rate  $Q$  is assumed to be constant. Note that only half of the  
 613 space is simulated due to geometric symmetry.

614 For cohesive elements, the coarse mesh density may reduce the accuracy  
 615 (Zielonka et al., 2014). Here we use a finer mesh (the smallest mesh size  
 616 around the hydraulic fracture path is  $0.5 \text{ cm}$ ) to circumvent this effect (Turon  
 617 et al., 2007; Ngo et al., 2019). All material parameters used in the simulation

Table A.1. Input material properties for the KGD model

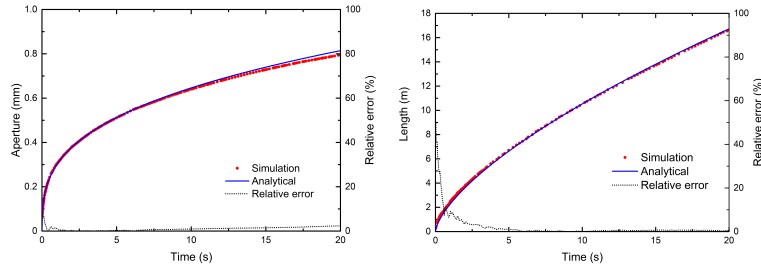
| Property           | Symbol   | Value   | Unit                            |
|--------------------|----------|---------|---------------------------------|
| Young's modulus    | $E$      | 17      | GPa                             |
| Poisson ratio      | $\nu$    | 0.2     | -                               |
| Fracture Energy    | $G_c$    | 120     | Pa·m                            |
| Tensile strength   | $\tau_c$ | 1.25    | MPa                             |
| Biot's coefficient | $b$      | 0.75    | -                               |
| Biot's Modulus     | $M_b$    | 68.7    | MPa                             |
| Permeability       | $k$      | 1.0e-16 | m <sup>2</sup>                  |
| Porosity           | $\phi$   | 0.2     | -                               |
| Fluid viscosity    | $\eta$   | 0.0001  | Pa·s                            |
| Injection rate     | $Q$      | 0.001   | m <sup>3</sup> ·s <sup>-1</sup> |

618 are given in Tab. A.1. According to Eq. (A.2), we obtain  $M = 0.0142$ ,  
619 indicating the toughness-dominated regime.

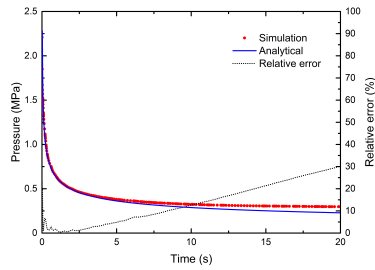
620 In this simulation, we perform 20 s of hydraulic stimulation. The frac-  
621 ture length, fracture aperture and pressure at the injection point, and the  
622 corresponding relative errors are given in Fig. A.2. Results show a good  
623 agreement between our numerical results and the analytical solutions ex-  
624 cept that the numerically obtained injection pressure has an increasing error  
625 as time increases. This is due to poro-elastic coupling effect (Carrier and  
626 Granet, 2012), which is not considered in the analytical model.

## 627 References

628 Aki, K., 1966. Generation and propagation of g waves from the niigata  
629 earthquake of june 16, 1964.: Part 2. estimation of earthquake moment,



(a) fracture aperture at injection point      (b) fracture length



(c) pressure at injection point

Fig. A.2. Comparison between analytical solutions and numerical simulations and the relative error

630 released energy, and stress-strain drop from the g wave spectrum. Bulletin  
 631 of the Earthquake Research Institute, University of Tokyo 44, 73–88. URL:  
 632 <https://ci.nii.ac.jp/naid/120000871042/en/>.

633 Albaric, J., Oye, V., Langet, N., Hasting, M., Lecomte, I., Iranpour, K.,  
 634 Messeiller, M., Reid, P., 2014. Monitoring of induced seismicity during the  
 635 first geothermal reservoir stimulation at paralana, australia. *Geothermics*  
 636 52, 120–131. doi:10.1016/j.geothermics.2013.10.013.

637 Baisch, S., Vörös, R., Rothert, E., Stang, H., Jung, R., Schellschmidt, R.,  
 638 2010. A numerical model for fluid injection induced seismicity at soultz-

- 639 sous-forêts. *International Journal of Rock Mechanics and Mining Sciences*  
640 47, 405–413. doi:10.1016/j.ijrmms.2009.10.001.
- 641 Barati, R., Liang, J.T., 2014. A review of fracturing fluid systems used  
642 for hydraulic fracturing of oil and gas wells. *Journal of Applied Polymer*  
643 *Science* 131. doi:10.1002/app.40735.
- 644 Barth, A., Wenzel, F., Langenbruch, C., 2013. Probability of earthquake oc-  
645 currence and magnitude estimation in the post shut-in phase of geothermal  
646 projects. *Journal of seismology* 17, 5–11. doi:10.1007/s10950-011-9260-9.
- 647 Baujard, C., Genter, A., Dalmais, E., Maurer, V., Hehn, R., Rosillette, R.,  
648 Vidal, J., Schmittbuhl, J., 2017. Hydrothermal characterization of wells  
649 grt-1 and grt-2 in rittershoffen, france: Implications on the understanding  
650 of natural flow systems in the rhine graben. *Geothermics* 65, 255–268.  
651 doi:10.1016/j.geothermics.2016.11.001.
- 652 Biot, M.A., 1941. General theory of three-dimensional consolidation. *Journal*  
653 *of applied physics* 12, 155–164. doi:10.1063/1.1712886.
- 654 Blöcher, G., Cacace, M., Jacquey, A.B., Zang, A., Heidbach, O., Hof-  
655 mann, H., Kluge, C., Zimmermann, G., 2018. Evaluating micro-seismic  
656 events triggered by reservoir operations at the geothermal site of groß  
657 schönebeck (germany). *Rock Mechanics and Rock Engineering* 51, 3265–  
658 3279. doi:10.1007/s00603-018-1521-2.
- 659 Brown, M.R., Ge, S., 2018. Small earthquakes matter in injection-  
660 induced seismicity. *Geophysical Research Letters* 45, 5445–5453.  
661 doi:10.1029/2018GL077472.

- 662 Brudzinski, M.R., Kozłowska, M., 2019. Seismicity induced by hydraulic  
663 fracturing and wastewater disposal in the appalachian basin, usa: A review.  
664 *Acta Geophysica* 67, 351–364. doi:10.1007/s11600-019-00249-7.
- 665 Cappa, F., Guglielmi, Y., Nussbaum, C., Birkholzer, J., 2018. On the rela-  
666 tionship between fault permeability increases, induced stress perturbation,  
667 and the growth of aseismic slip during fluid injection. *Geophysical Research*  
668 *Letters* 45, 11–012. doi:10.1029/2018GL080233.
- 669 Carrier, B., Granet, S., 2012. Numerical modeling of hydraulic fracture  
670 problem in permeable medium using cohesive zone model. *Engineering*  
671 *fracture mechanics* 79, 312–328. doi:10.1016/j.engfracmech.2011.11.012.
- 672 Chang, K., Segall, P., 2016. Injection-induced seismicity on basement faults  
673 including poroelastic stressing. *Journal of Geophysical Research: Solid*  
674 *Earth* 121, 2708–2726. doi:10.1002/2015JB012561.
- 675 Chang, K.W., Yoon, H., Martinez, M.J., 2018. Seismicity rate surge on  
676 faults after shut-in: Poroelastic response to fluid injection. *Bulletin of the*  
677 *Seismological Society of America* 108, 1889–1904. doi:10.1785/0120180054.
- 678 Chen, Z., Jeffrey, R.G., Zhang, X., Kear, J., et al., 2017. Finite-element  
679 simulation of a hydraulic fracture interacting with a natural fracture. *Spe*  
680 *Journal* 22, 219–234. doi:10.2118/176970-PA.
- 681 Colmenares, L.B., Zoback, M.D., 2007. Hydraulic fracturing and wellbore  
682 completion of coalbed methane wells in the powder river basin, wyoming:  
683 implications for water and gas production. *AAPG bulletin* 91, 51–67.  
684 doi:10.1306/07180605154.

- 685 Cornet, F., Jianmin, Y., 1995. Analysis of induced seismicity for stress field  
686 determination and pore pressure mapping, in: *Mechanics Problems in Geo-*  
687 *dynamics Part I*. Springer, pp. 677–700.
- 688 Coussy, O., 2004. *Poromechanics*. John Wiley & Sons.
- 689 De Barros, L., Cappa, F., Guglielmi, Y., Duboeuf, L., Grasso, J.R., 2019.  
690 Energy of injection-induced seismicity predicted from in-situ experiments.  
691 *Scientific reports* 9, 1–11. doi:10.1038/s41598-019-41306-x.
- 692 De Simone, S., Carrera, J., Vilarrasa, V., 2017. Superposition approach  
693 to understand triggering mechanisms of post-injection induced seismicity.  
694 *Geothermics* 70, 85–97. doi:10.1016/j.geothermics.2017.05.011.
- 695 Deng, Q., Blöcher, G., Cacace, M., Schmittbuhl, J., 2021. Hydraulic dif-  
696 fusivity of a partially open rough fracture. *Rock Mechanics and Rock*  
697 *Engineering* , 1–23.
- 698 Detournay, E., 2004. Propagation regimes of fluid-driven fractures in  
699 impermeable rocks. *International Journal of Geomechanics* 4, 35–45.  
700 doi:10.1061/(ASCE)1532-3641(2004)4:1(35).
- 701 Ellsworth, W.L., 2013. Injection-induced earthquakes. *Science* 341, 1225942.  
702 doi:10.1126/science.1225942.
- 703 Evans, J.P., Forster, C.B., Goddard, J.V., 1997. Permeability of fault-related  
704 rocks, and implications for hydraulic structure of fault zones. *Journal of*  
705 *structural Geology* 19, 1393–1404. doi:10.1016/S0191-8141(97)00057-6.

- 706 Evans, K.F., Moriya, H., Niitsuma, H., Jones, R., Phillips, W., Genter, A.,  
707 Sausse, J., Jung, R., Baria, R., 2005. Microseismicity and permeability  
708 enhancement of hydrogeologic structures during massive fluid injections  
709 into granite at 3 km depth at the soultz HDR site. *Geophysical Journal*  
710 *International* 160, 388–412. doi:10.1111/j.1365-246X.2004.02474.x.
- 711 Evans, K.F., Zappone, A., Kraft, T., Deichmann, N., Moia, F.,  
712 2012. A survey of the induced seismic responses to fluid injection  
713 in geothermal and CO<sub>2</sub> reservoirs in Europe. *Geothermics* 41, 30–54.  
714 doi:10.1016/j.geothermics.2011.08.002.
- 715 Fehler, M.C., 1989. Stress control of seismicity patterns observed during  
716 hydraulic fracturing experiments at the Fenton Hill hot dry rock geother-  
717 mal energy site, New Mexico, in: *International Journal of Rock Mechanics*  
718 *and Mining Sciences & Geomechanics Abstracts*, Elsevier. pp. 211–219.  
719 doi:10.1016/0148-9062(89)91971-2.
- 720 Garagash, D.I., 2006. Plane-strain propagation of a fluid-driven fracture  
721 during injection and shut-in: Asymptotics of large toughness. *Engineering*  
722 *Fracture Mechanics* 73, 456–481. doi:10.1016/j.engfracmech.2005.07.012.
- 723 Gaucher, E., Schoenball, M., Heidbach, O., Zang, A., Fokker, P., van Wees,  
724 J.D., Kohl, T., 2015. Induced seismicity in geothermal reservoirs: physical  
725 processes and key parameters, in: *World Geothermal Congress 2015*.
- 726 Gu, H., Weng, X., Lund, J.B., Mack, M.G., Ganguly, U., Suarez-Rivera, R.,  
727 et al., 2012. Hydraulic fracture crossing natural fracture at nonorthogonal

- 728 angles: a criterion and its validation. *SPE Production & Operations* 27,  
729 20–26. doi:10.2118/139984-PA.
- 730 Guglielmi, Y., Cappa, F., Avouac, J.P., Henry, P., Elsworth, D., 2015. Seis-  
731 micity triggered by fluid injection-induced aseismic slip. *Science* 348, 1224–  
732 1226. doi:10.1126/science.aab0476.
- 733 Hanks, T.C., Kanamori, H., 1979. A moment magnitude scale.  
734 *Journal of Geophysical Research: Solid Earth* 84, 2348–2350.  
735 doi:10.1029/JB084iB05p02348.
- 736 Häring, M.O., Schanz, U., Ladner, F., Dyer, B.C., 2008. Characterisation  
737 of the basel 1 enhanced geothermal system. *Geothermics* 37, 469–495.  
738 doi:10.1016/j.geothermics.2008.06.002.
- 739 Hearn, E.H., Koltermann, C., Rubinstein, J.L., 2018. Numerical models of  
740 pore pressure and stress changes along basement faults due to wastewater  
741 injection: Applications to the 2014 milan, kansas earthquake. *Geochem-*  
742 *istry, Geophysics, Geosystems* 19, 1178–1198. doi:10.1002/2017GC007194.
- 743 Hofmann, H., Zimmermann, G., Zang, A., Min, K.B., 2018. Cyclic soft  
744 stimulation (css): a new fluid injection protocol and traffic light system  
745 to mitigate seismic risks of hydraulic stimulation treatments. *Geothermal*  
746 *Energy* 6, 27. doi:10.1186/s40517-018-0114-3.
- 747 Howard, G.C., Fast, C., 1957. Optimum fluid characteristics for fracture  
748 extension, in: *Drilling and production practice*, OnePetro.



- 749 Hsieh, P.A., Bredehoeft, J.D., 1981. A reservoir analysis of the denver earth-  
750 quakes: A case of induced seismicity. *Journal of Geophysical Research:*  
751 *Solid Earth* 86, 903–920. doi:10.1029/JB086iB02p00903.
- 752 Jacquey, A.B., Urpi, L., Cacace, M., Blöcher, G., Zimmermann, G.,  
753 Scheck-Wenderoth, M., 2018. Far field poroelastic response of geother-  
754 mal reservoirs to hydraulic stimulation treatment: Theory and appli-  
755 cation at the groß schönebeck geothermal research facility. *Interna-*  
756 *tional Journal of Rock Mechanics and Mining Sciences* 110, 316–327.  
757 doi:10.1016/j.ijrmms.2018.08.012.
- 758 Jaeger, J.C., Cook, N.G., Zimmerman, R., 2009. *Fundamentals of rock me-*  
759 *chanics*. John Wiley & Sons.
- 760 Ji, Y., Wu, W., Zhao, Z., 2019. Unloading-induced rock fracture activa-  
761 tion and maximum seismic moment prediction. *Engineering Geology* 262,  
762 105352. doi:10.1016/j.enggeo.2019.105352.
- 763 Johri, M., Zoback, M.D., 2013. The evolution of stimulated reservoir  
764 volume during hydraulic stimulation of shale gas formations, in: *Un-*  
765 *conventional Resources Technology Conference*, Society of Exploration  
766 Geophysicists, American Association of Petroleum . . . . pp. 1661–1671.  
767 doi:10.1190/urtec2013-170.
- 768 Keranen, K.M., Weingarten, M., Abers, G.A., Bekins, B.A., Ge, S.,  
769 2014. Sharp increase in central oklahoma seismicity since 2008  
770 induced by massive wastewater injection. *Science* 345, 448–451.  
771 doi:10.1126/science.1255802.

- 772 Kettlety, T., Verdon, J., Werner, M., Kendall, J., 2020. Stress transfer from  
773 opening hydraulic fractures controls the distribution of induced seismic-  
774 ity. *Journal of Geophysical Research: Solid Earth* 125, e2019JB018794.  
775 doi:10.1029/2019JB018794.
- 776 Krietsch, H., Villiger, L., Doetsch, J., Gischig, V., Evans, K.F., Brixel,  
777 B., Jalali, M., Loew, S., Giardini, D., Amann, F., 2020. Changing flow  
778 paths caused by simultaneous shearing and fracturing observed during hy-  
779 draulic stimulation. *Geophysical Research Letters* 47, e2019GL086135.  
780 doi:10.1029/2019GL086135.
- 781 Langenbruch, C., Weingarten, M., Zoback, M.D., 2018. Physics-based fore-  
782 casting of man-made earthquake hazards in oklahoma and kansas. *Nature*  
783 *communications* 9, 1–10. doi:10.1038/s41467-018-06167-4.
- 784 Law, B.E., Spencer, C.W., Howell, D., Wiese, K., Fanelli, M., Zink, L.,  
785 Cole, F., 1993. Gas in tight reservoirs—an emerging major source of  
786 energy. *US Geological Survey Professional Paper* 1570, 233–252. URL:  
787 <https://www.osti.gov/biblio/6814307>.
- 788 Lecampion, B., Bungler, A., Zhang, X., 2018. Numerical methods for hy-  
789 draulic fracture propagation: a review of recent trends. *Journal of natural*  
790 *gas science and engineering* 49, 66–83. doi:10.1016/j.jngse.2017.10.012.
- 791 Lee, K.K., Ellsworth, W.L., Giardini, D., Townend, J., Ge, S., Shi-  
792 mamoto, T., Yeo, I.W., Kang, T.S., Rhie, J., Sheen, D.H., et al.,  
793 2019. Managing injection-induced seismic risks. *Science* 364, 730–732.  
794 doi:10.1126/science.aax1878.

- 795 Lei, Q., Doonechaly, N.G., Tsang, C.F., 2021. Modelling fluid  
796 injection-induced fracture activation, damage growth, seismicity occur-  
797 rence and connectivity change in naturally fractured rocks. *Internation-*  
798 *ational Journal of Rock Mechanics and Mining Sciences* 138, 104598.  
799 doi:10.1016/j.ijrmms.2020.104598.
- 800 Lei, X., Huang, D., Su, J., Jiang, G., Wang, X., Wang, H., Guo, X., Fu,  
801 H., 2017. Fault reactivation and earthquakes with magnitudes of up to  
802 mw4. 7 induced by shale-gas hydraulic fracturing in sichuan basin, china.  
803 *Scientific reports* 7, 1–12. doi:10.1038/s41598-017-08557-y.
- 804 Lei, X., Wang, Z., Su, J., 2019. The december 2018 ml 5.7 and jan-  
805 uary 2019 ml 5.3 earthquakes in south sichuan basin induced by shale  
806 gas hydraulic fracturing. *Seismological Research Letters* 90, 1099–1110.  
807 doi:10.1785/0220190029.
- 808 Lengliné, O., Boubacar, M., Schmittbuhl, J., 2017. Seismicity related to the  
809 hydraulic stimulation of grt1, rittershoffen, france. *Geophysical Journal*  
810 *International* 208, 1704–1715. doi:10.1093/gji/ggw490.
- 811 Li, Y., Deng, J., Liu, W., Feng, Y., 2017. Modeling hydraulic  
812 fracture propagation using cohesive zone model equipped with fric-  
813 tional contact capability. *Computers and geotechnics* 91, 58–70.  
814 doi:10.1016/j.compgeo.2017.07.001.
- 815 Liu, Y., Guo, J., Chen, Z., 2016. Leakoff characteristics and an equivalent  
816 leakoff coefficient in fractured tight gas reservoirs. *Journal of Natural Gas*  
817 *Science and Engineering* 31, 603–611.

- 818 Majer, E.L., Baria, R., Stark, M., Oates, S., Bommer, J.,  
819 Smith, B., Asanuma, H., 2007. Induced seismicity associated  
820 with enhanced geothermal systems. *Geothermics* 36, 185–222.  
821 doi:10.1016/j.geothermics.2007.03.003.
- 822 Maurer, J., Dunham, E.M., Segall, P., 2020. Role of fluid injection on earth-  
823 quake size in dynamic rupture simulations on rough faults. *Geophysical*  
824 *Research Letters* 47, e2020GL088377. doi:10.1029/2020GL088377.
- 825 McClure, M.W., 2015. Generation of large postinjection-induced seismic  
826 events by backflow from dead-end faults and fractures. *Geophysical Re-*  
827 *search Letters* 42, 6647–6654. doi:10.1002/2015GL065028.
- 828 McClure, M.W., Horne, R.N., 2011. Investigation of injection-induced seis-  
829 micity using a coupled fluid flow and rate/state friction model. *Geophysics*  
830 76, WC181–WC198. doi:10.1190/geo2011-0064.1.
- 831 McDaniel, B., et al., 1990. Hydraulic fracturing techniques used for stimula-  
832 tion of coalbed methane wells, in: SPE Eastern Regional Meeting, Society  
833 of Petroleum Engineers. doi:10.2118/21292-MS.
- 834 Meyer, G., Baujard, C., Hehn, R., Genter, A., McClure, M., 2017. Analysis  
835 and numerical modelling of pressure drops observed during hydraulic stim-  
836 ulation of grt-1 geothermal well (rittershoffen, france). *Proc 42nd Work*  
837 *Geotherm Reserv Eng* , 14.
- 838 Mitchell, T., Faulkner, D., 2012. Towards quantifying the matrix perme-  
839 ability of fault damage zones in low porosity rocks. *Earth and Planetary*  
840 *Science Letters* 339, 24–31. doi:10.1016/j.epsl.2012.05.014.

- 841 Mukuhira, Y., Asanuma, H., Niitsuma, H., Häring, M.O., 2013. Charac-  
842 teristics of large-magnitude microseismic events recorded during and after  
843 stimulation of a geothermal reservoir at basel, switzerland. *Geothermics*  
844 45, 1–17. doi:10.1016/j.geothermics.2012.07.005.
- 845 Mukuhira, Y., Dinske, C., Asanuma, H., Ito, T., Häring, M., 2017. Pore  
846 pressure behavior at the shut-in phase and causality of large induced seis-  
847 micity at basel, switzerland. *Journal of Geophysical Research: Solid Earth*  
848 122, 411–435. doi:10.1002/2016JB013338.
- 849 Murphy, H., Brown, D., Jung, R., Matsunaga, I., Parker, R., 1999. Hy-  
850 draulics and well testing of engineered geothermal reservoirs. *Geothermics*  
851 28, 491–506. doi:10.1016/S0375-6505(99)00025-5.
- 852 Nara, Y., Meredith, P.G., Yoneda, T., Kaneko, K., 2011. Influence of  
853 macro-fractures and micro-fractures on permeability and elastic wave  
854 velocities in basalt at elevated pressure. *Tectonophysics* 503, 52–59.  
855 doi:10.1016/j.tecto.2010.09.027.
- 856 Ngo, D.T., Pellet, F.L., Bruel, D., 2019. Modeling of fault slip dur-  
857 ing hydraulic stimulation in a naturally fractured medium. *Geome-  
858 chanics and Geophysics for Geo-Energy and Geo-Resources* 5, 237–251.  
859 doi:10.1007/s40948-019-00108-1.
- 860 Norbeck, J.H., McClure, M.W., Horne, R.N., 2018. Field obser-  
861 vations at the fenton hill enhanced geothermal system test site  
862 support mixed-mechanism stimulation. *Geothermics* 74, 135–149.  
863 doi:10.1016/j.geothermics.2018.03.003.

- 864 Norbeck, J.H., McClure, M.W., Lo, J.W., Horne, R.N., 2016. An em-  
865 bedded fracture modeling framework for simulation of hydraulic frac-  
866 turing and shear stimulation. *Computational Geosciences* 20, 1–18.  
867 doi:10.1007/s10596-015-9543-2.
- 868 Parotidis, M., Shapiro, S.A., Rothert, E., 2004. Back front of seismicity  
869 induced after termination of borehole fluid injection. *Geophysical Research*  
870 *Letters* 31. doi:10.1029/2003GL018987.
- 871 Passelègue, F.X., Almakari, M., Dublanchet, P., Barras, F., Fortin, J., Violay,  
872 M., 2020. Initial effective stress controls the nature of earthquakes. *Nature*  
873 *communications* 11, 1–8. doi:10.1038/s41467-020-18937-0.
- 874 Passelègue, F.X., Brantut, N., Mitchell, T.M., 2018. Fault reactivation by  
875 fluid injection: controls from stress state and injection rate. *Geophysical*  
876 *Research Letters* 45, 12–837. doi:10.1029/2018GL080470.
- 877 Pearson, C., 1981. The relationship between microseismicity and high pore  
878 pressures during hydraulic stimulation experiments in low permeability  
879 granitic rocks. *Journal of Geophysical Research: Solid Earth* 86, 7855–  
880 7864. doi:10.1029/JB086iB09p07855.
- 881 Piris, G., Griera, A., Gomez-Rivas, E., Herms, I., McClure, M.W., Norbeck,  
882 J.H., 2018. Fluid pressure drops during stimulation of segmented faults in  
883 deep geothermal reservoirs. *Geothermal Energy* 6, 24. doi:10.1186/s40517-  
884 018-0110-7.
- 885 Ren, L., Lin, R., Zhao, J.z., Yang, K.w., Hu, Y.q., Wang, X.j., 2015. Simul-  
886 taneous hydraulic fracturing of ultra-low permeability sandstone reservoirs

- 887 in china: Mechanism and its field test. *Journal of Central South University*  
888 22, 1427–1436. doi:10.1007/s11771-015-2660-1.
- 889 Rutqvist, J., Rinaldi, A.P., Cappa, F., Moridis, G.J., 2013. Modeling of fault  
890 reactivation and induced seismicity during hydraulic fracturing of shale-  
891 gas reservoirs. *Journal of Petroleum Science and Engineering* 107, 31–44.  
892 doi:10.1016/j.petrol.2013.04.023.
- 893 Saadat, M., Taheri, A., 2019. A cohesive discrete element based  
894 approach to characterizing the shear behavior of cohesive soil and  
895 clay-infilled rock joints. *Computers and Geotechnics* 114, 103109.  
896 doi:10.1016/j.compgeo.2019.103109.
- 897 Schill, E., Genter, A., Cuenot, N., Kohl, T., 2017. Hydraulic performance his-  
898 tory at the soultz egs reservoirs from stimulation and long-term circulation  
899 tests. *Geothermics* 70, 110–124. doi:10.1016/j.geothermics.2017.06.003.
- 900 Shapiro, S.A., Audigane, P., Royer, J.J., 1999. Large-scale in situ perme-  
901 ability tensor of rocks from induced microseismicity. *Geophysical Journal*  
902 *International* 137, 207–213. doi:10.1046/j.1365-246x.1999.00781.x.
- 903 Stanchits, S., Mayr, S., Shapiro, S., Dresen, G., 2011. Fracturing of  
904 porous rock induced by fluid injection. *Tectonophysics* 503, 129–145.  
905 doi:10.1016/j.tecto.2010.09.022.
- 906 Turon, A., Davila, C.G., Camanho, P.P., Costa, J., 2007. An engineer-  
907 ing solution for mesh size effects in the simulation of delamination us-  
908 ing cohesive zone models. *Engineering fracture mechanics* 74, 1665–1682.  
909 doi:10.1016/j.engfracmech.2006.08.025.

- 910 Ucar, E., Berre, I., Keilegavlen, E., 2017. Postinjection normal closure of  
911 fractures as a mechanism for induced seismicity. *Geophysical Research*  
912 *Letters* 44, 9598–9606. doi:10.1002/2017GL074282.
- 913 Wang, J., Elsworth, D., Denison, M.K., 2018. Hydraulic fracturing  
914 with leakoff in a pressure-sensitive dual porosity medium. *Interna-*  
915 *tional Journal of Rock Mechanics and Mining Sciences* 107, 55–68.  
916 doi:10.1016/j.ijrmms.2018.04.042.
- 917 Wang, L., Kwiatek, G., Rybacki, E., Bohnhoff, M., Dresen, G., 2020.  
918 Injection-induced seismic moment release and laboratory fault slip: Im-  
919 plications for fluid-induced seismicity. *Geophysical Research Letters* 47,  
920 e2020GL089576. doi:10.1029/2020GL089576.
- 921 Xie, L., Min, K.B., 2016. Initiation and propagation of fracture shearing  
922 during hydraulic stimulation in enhanced geothermal system. *Geothermics*  
923 59, 107–120. doi:10.1016/j.geothermics.2015.10.012.
- 924 Yao, Y., 2012. Linear elastic and cohesive fracture analysis to model hydraulic  
925 fracture in brittle and ductile rocks. *Rock mechanics and rock engineering*  
926 45, 375–387. doi:10.1007/s00603-011-0211-0.
- 927 Ye, Z., Ghassemi, A., 2018. Injection-induced shear slip and permeability  
928 enhancement in granite fractures. *Journal of Geophysical Research: Solid*  
929 *Earth* 123, 9009–9032. doi:10.1029/2018JB016045.
- 930 Yeo, I., Brown, M., Ge, S., Lee, K., 2020. Causal mechanism of injection-  
931 induced earthquakes through the m w 5.5 pohang earthquake case study.  
932 *Nature communications* 11, 1–12. doi:10.1038/s41467-020-16408-0.



- 933 Yoon, J.S., Stephansson, O., Zang, A., Min, K.B., Lanaro, F., 2017. Dis-  
934 crete bonded particle modelling of fault activation near a nuclear waste  
935 repository site and comparison to static rupture earthquake scaling laws.  
936 International Journal of Rock Mechanics and Mining Sciences 98, 1–9.  
937 doi:10.1016/j.ijrmms.2017.07.008.
- 938 Zang, A., Zimmermann, G., Hofmann, H., Stephansson, O., Min, K.B., Kim,  
939 K.Y., 2019. How to reduce fluid-injection-induced seismicity. Rock Me-  
940chanics and Rock Engineering 52, 475–493. doi:10.1007/s00603-018-1467-4.
- 941 Zhuang, L., Kim, K.Y., Jung, S.G., Diaz, M., Min, K.B., Zang, A., Stephans-  
942 son, O., Zimmermann, G., Yoon, J.S., Hofmann, H., 2019. Cyclic hy-  
943 draulic fracturing of pocheon granite cores and its impact on break-  
944 down pressure, acoustic emission amplitudes and injectivity. Interna-  
945 tional Journal of Rock Mechanics and Mining Sciences 122, 104065.  
946 doi:10.1016/j.ijrmms.2019.104065.
- 947 Zhuang, X., Chun, J., Zhu, H., 2014. A comparative study on unfilled and  
948 filled crack propagation for rock-like brittle material. Theoretical and Ap-  
949 plied Fracture Mechanics 72, 110–120. doi:10.1016/j.tafmec.2014.04.004.
- 950 Zielonka, M.G., Searles, K.H., Ning, J., Buechler, S.R., 2014. Development  
951 and validation of fully-coupled hydraulic fracturing simulation capabilities,  
952 in: Proceedings of the SIMULIA community conference, SCC2014, pp. 19–  
953 21.
- 954 Zoback, M., Rummel, F., Jung, R., Raleigh, C., 1977. Laboratory hydraulic  
955 fracturing experiments in intact and pre-fractured rock, in: International

- 956 Journal of Rock Mechanics and Mining Sciences & Geomechanics Ab-  
957 stracts, Elsevier. pp. 49–58. doi:10.1016/0148-9062(77)90196-6.
- 958 Zoback, M.D., 2010. Reservoir geomechanics. Cambridge University Press.  
959 doi:10.1017/CBO9780511586477.
- 960 Zoback, M.D., Gorelick, S.M., 2012. Earthquake triggering and large-scale  
961 geologic storage of carbon dioxide. Proceedings of the National Academy  
962 of Sciences 109, 10164–10168. doi:10.1073/pnas.1202473109.

**Cacace:** Reviewing and Editing, Validation. **Jean Schmittbuhl:** Supervision.

**Declaration of interests**

The authors declare that they have no known competing financial interests or personal relationships that could have appeared to influence the work reported in this paper.

The authors declare the following financial interests/personal relationships which may be considered as potential competing interests:

1 Modeling of fluid-induced seismicity during injection  
2 and after shut-in

3 Qinglin Deng<sup>1,\*</sup>, Guido Blöcher<sup>2</sup>, Mauro Cacace<sup>2</sup>, Jean Schmittbuhl<sup>1</sup>

---

---

4 Highlights

5 **Modeling of fluid-induced seismicity during injection and after**  
6 **shut-in**

7 Qinglin Deng, Guido Blöcher, Mauro Cacace, Jean Schmittbuhl

- 8 • A fully hydro-mechanical model is to capture fault slip behavior during  
9 injection and after shut-in
- 10 • Reproduce fluid induced fault slip after shut-in with no hydraulic con-  
11 nection and with obvious time lag
- 12 • Coupled pressure diffusion with poro-elastic stressing can be responsi-  
13 ble for the larger magnitude events after shut-in than during injection
- 14 • Initial stress state is of central importance for fluid injection induced  
15 seismicity

---

\*Corresponding author

*Email address:* [dengq@unistra.fr](mailto:dengq@unistra.fr) (Qinglin Deng)

<sup>1</sup>EOST/ITES, Université de Strasbourg/CNRS, France

<sup>2</sup>GFZ German Research Centre for Geosciences, Potsdam, Germany